Geoscience Frontiers 14 (2023) 101610

Contents lists available at ScienceDirect

Geoscience Frontiers

journal homepage: www.elsevier.com/locate/gsf

Research Paper

# Cenozoic low temperature cooling history of the eastern Lhasa terrane: Implications for high-relief topography of external drainage area in the southern Tibetan Plateau

Wenbo Su [a], Zhiyuan He [a,*], Linglin Zhong [b], Stijn Glorie [c], Kanghui Zhong [b], Johan De Grave [a]

[a] Laboratory for Mineralogy and Petrology, Department of Geology, Ghent University, Krijgslaan 281 S8, 9000 Ghent, Belgium
[b] College of Earth Sciences, Chengdu University of Technology, Chengdu 610059, China
[c] Department of Earth Sciences, School of Physical Sciences, The University of Adelaide, SA-5005, Australia

ARTICLE INFO

*Article history:*
Received 21 September 2022
Revised 14 March 2023
Accepted 31 March 2023
Available online 5 April 2023
Handling Editor: Nick Roberts

*Keywords:*
Cenozoic
Apatite fission track thermochronology
Exhumation
Lhasa terrane
External drainage area
Tibetan Plateau

ABSTRACT

The Tibetan Plateau geographically contains internal and external drainage areas based on the distributions of river flows and catchments. The internal and external drainage areas display similar high-elevations, while their topographic reliefs are not comparable; the former shows a large low-relief surface, whereas the latter is characterized by relatively high relief. The eastern Lhasa terrane is a key tectonic component of the Tibetan Plateau. It is characterized by high topography and relief, but the thermal history of its basement remains relatively poorly constrained. In this study we report new apatite fission track data from the eastern part of the central Lhasa terrane to constrain the thermo-tectonic evolution of the external drainage area in the southern Tibetan Plateau. Twenty-one new AFT ages and associated thermal history models reveal that the basement underlying the external drainage area in southern Tibet experienced three main phases of rapid cooling in the Cenozoic. The Paleocene-early Eocene (~60–48 Ma) cooling was likely induced by crustal shortening and associated rock exhumation, due to accelerated northward subduction of the NeoTethys oceanic lithosphere. A subsequent cooling pulse lasted from the late Eocene to early Oligocene (~40–28 Ma), possibly due to the thickening and consequential erosion of the Lhasa lithosphere resulted from the continuous northward indentation of the India plate into Eurasia. The most recent rapid cooling event occurred in the middle Miocene-early Pliocene (~16–4 Ma), likely induced by accelerated incision of the Lhasa River and local thrust faulting. Our AFT ages and published low-temperature thermochronological data reveal that the external drainage area experienced younger cooling events compared with the internal drainage area, and that the associated differentiated topographic evolution initiated at ca. 30 Ma. The contributing factors for the formation of the high-relief topography mainly contain active surface uplift, fault activity, and the enhanced incision of the Yarlung River.



## 1. Introduction

The development of topographic relief in an active orogenic belt is associated with the interaction between tectonic processes occurring in the deep earth, at the surface (e.g., subsidence and development of river systems) and the evolving climate (Cloetingh et al., 2007). Exploring the coupling of tectonics, surface erosion and climate change is always of great importance when studying the intricate evolution of continental topography (Willett et al., 2006; Whipple, 2009; Liu-Zeng et al., 2018a).

The Tibetan Plateau is the highest and largest topographic feature on Earth, it covers an area of approximately 3500 km by 1500 km, containing 82 % of the world's land surface areas that are >4 km above sea level (Fielding et al., 1994). One prominent feature of the Tibetan Plateau is its high-elevation low-relief topography (Fielding et al., 1994; Liu-Zeng et al., 2008). However, the relief is not uniform across the plateau. The majority of the plateau interior has low-relief topography with internal drainage in absence of outflowing rivers (Fig. 1). In contrast, some regions outside the internal drainage area, especially at the Plateau's edges, such as the eastern Lhasa and Qiangtang terranes, display a relatively high-relief topography (Fig. 1; Fielding et al., 1994; Liu-Zeng et al., 2008). These areas have external drainage by a number

* Corresponding author.
*E-mail addresses:* Zhiyuan.He@UGent.be, hezhiyuan@smail.nju.edu.cn (Z. He).

https://doi.org/10.1016/j.gsf.2023.101610

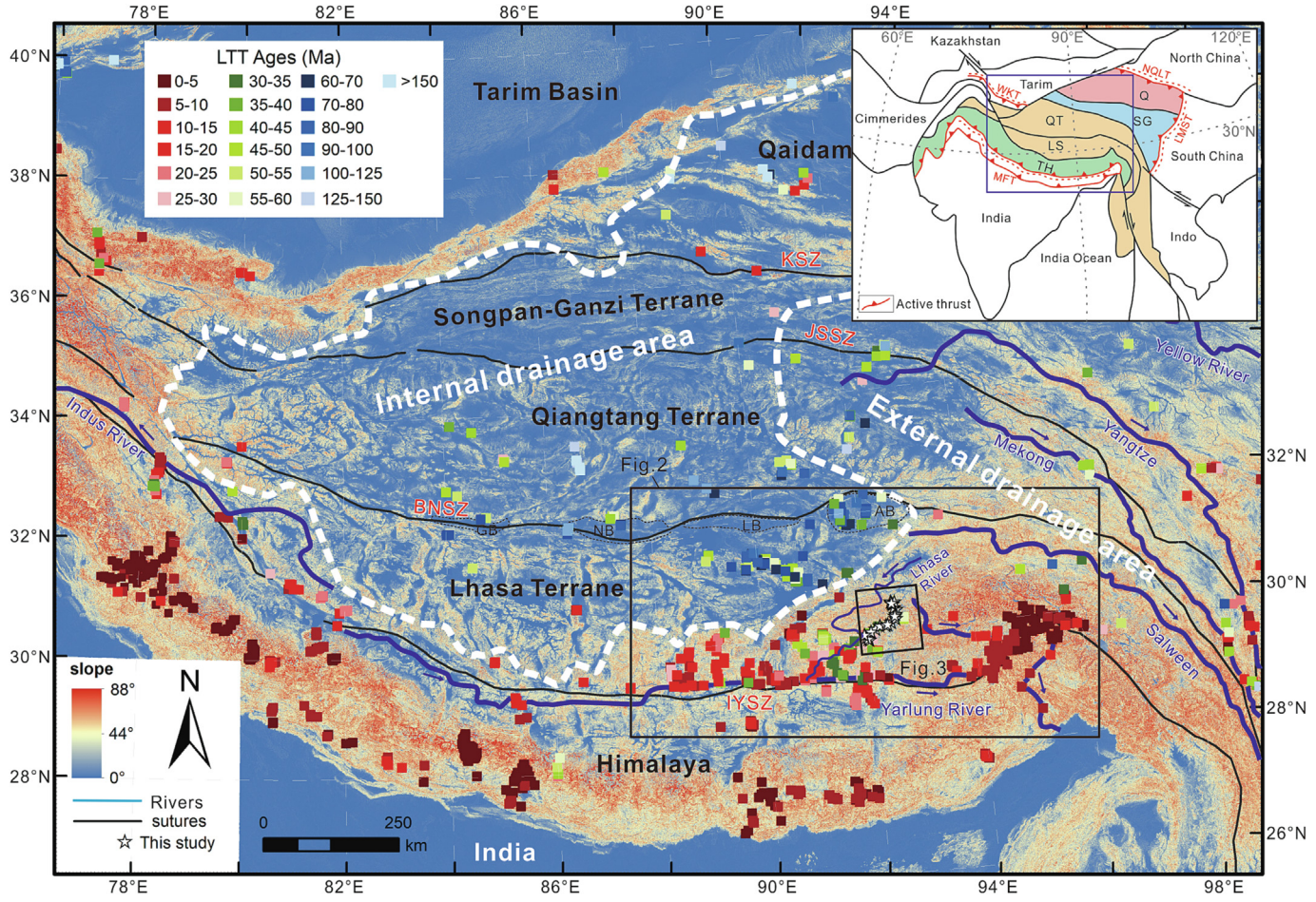


**Fig. 1.** Geologic and geomorphic framework of the Tibetan Plateau. Tectonic features are from Tapponnier et al. (2001) and Pan et al. (2004). Slope distribution was calculated using SRTMSLOPE images with a 90 m/pixel resolution. The white dashed line contours the modern internally drained area of the Tibetan Plateau (Liu-Zeng et al., 2008; Strobl et al., 2012). Black lines are sutures zones: BNSZ = Bangong-Nujang suture zone; IYSZ = Indus-Yarlung suture zone; JSSZ = Jinsha suture zone; KSZ = Kunlun suture zone. The black dashed lines delineate specific geological units. AB = Anduo basement; GB = Gaize basin; LB = Lunpola basin; NB = Nima basin. LTT ages (Ma) indicate "Low-temperature thermochronometric ages (Ma)". All LTT ages are listed in the Supplementary Data Table S1. LMST = Longmenshan thrust; LS = Lhasa; MFT = Main Frontal thrust; NQLT = North Qilian thrust; Q = Qaidam; QT = Qiangtang; SG = Songpan-Ganzi; TH = Tethyan Himalaya; WKT = West Kunlun thrust.

of large river systems [e.g., the Yarlung, Salween (Nu), Mekong (Lancang) and Yangtze Rivers], carrying massive volumes of sediments from the Tibetan Plateau margins to the Indian ocean (Fig. 1). Previous studies have focused more on the formation processes of the high-elevation low-relief geomorphic features in the internal drainage area. Here, some researchers suggest that the northern Lhasa terrane has attained a broad low-relief surface during the early stages of the India-Asia collision (Hetzel et al., 2011; Haider et al., 2013). Simultaneously, at ca. 45 Ma, the northern Lhasa and Qiangtang terranes formed a high-elevation topography (Rohrmann et al., 2012). However, previous studies found that a topographic depression that includes the Nima–Lunpola–Garze basins, with elevations lower than 2.0 km, probably existed in the northern Lhasa terrane in the Eocene (e.g., Xu et al., 2015; Su et al., 2020; Xiong et al., 2022). The surface of this depression was uplifted to its present elevation (>4.0 km) around ~29–26 Ma ago, resulting in the formation of the regional proto-plateau (Rowley and Currie, 2006; DeCelles et al., 2007; Fang et al., 2020; Su et al., 2020; Ding et al., 2022; Xiong et al., 2022). Contemporaneously, the low-relief landscape of the depression also developed as indicated by low-temperature thermochronological data and sedimentary provenance analyses, due to mantle flow or tectonic quiescence in an arid environment (Han et al., 2019; Li et al., 2022; Xue et al., 2022).

In the contiguous external drainage area, such as the eastern Lhasa and Qiangtang terranes, the topographic relief is comparatively high and quite different from that of the internal drainage region (Figs. 1 and 2). So far, a series of studies have been conducted to constrain the tectonic and topographic evolution of eastern Tibet, which displays unique high-elevation, low-relief 'relict' landscapes (e.g., Clark et al., 2006; Yuan et al., 2021; Cao et al., 2022). By comparison, little attention has been paid to how the contrasting topography developed in southern Tibet, although it represents a distinct geomorphic feature with high significance for understanding the topographic history of the Tibetan Plateau. In this work, we study the morpho-tectonic evolution of the unique, relatively high-relief external drainage area in the plateau, by taking the eastern Lhasa terrane as a representative example. In an effort to constrain the complex topography development in this region, we applied apatite fission track (AFT) thermochronology, which is sensitive to near surface (<~2–4 km) deformation and erosion processes (Green et al., 1989; Wagner and Van den haute, 1992; Reiners and Ehlers, 2005). In order to gain a more comprehensive understanding of the morpho-tectonic evolution of the external drainage area in the southern Tibetan Plateau, both samples from deeply incised river valleys and from locations distal to rivers and faults were studied. Combined with published low-temperature thermochronological (LTT) data from the Lhasa and

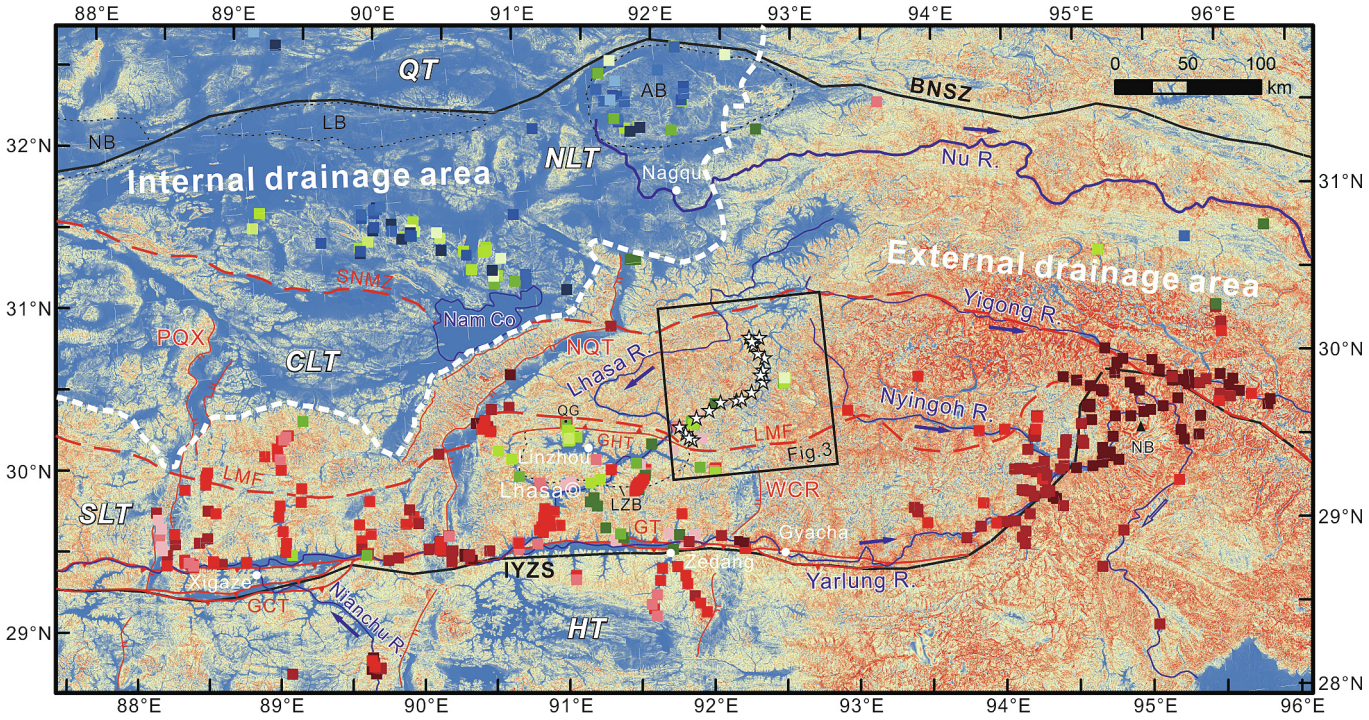


**Fig. 2.** Geologic and geomorphic framework of the eastern Lhasa terrane. Map key, symbols, and low-temperature thermochronological ages same as in Fig. 1. Tectonic features are from Pan et al. (2004) and Zhu et al. (2013). The black lines represent the same sutures zones as in Fig. 1. HT = Himalaya terrane; QT = Qiangtang terrane. The red dashed lines are the fault or suture zone that sub-divides the Lhasa terrane into three sub-terranes. CLT = central Lhasa terrane; LMF = Luobadui-Milashan fault; NLT = northern Lhasa terrane; SLT = southern Lhasa terrane; SNMZ = Shiquan River-Nam Tso mélange zone. The red lines are thrusts and north-striking normal faults. GCT = Great Counter thrust; GT = Gangdese thrust; NQT = Nyainqentanghla fault; PQX = Pum Qu-Xainza rift; WCF = Woka-Cuona fault. LZB = Linzhou basin; NB = Namche-Barwa; QG = Qianggeren granite; R. = River. (For interpretation of the references to colour in this figure legend, the reader is referred to the web version of this article.)

Qiangtang terranes, we tried to decipher the thermo-tectonic evolution of the eastern Lhasa terrane, and the timing of the development of high-relief topography of the studied external drainage area as well.

## 2. Geological setting

The Tibetan Plateau consists of four ~E–W trending terranes, which are, from north to south, the Songpan-Ganzi, Qiangtang, Lhasa and Tethyan Himalaya terranes (Fig. 1). The Lhasa terrane is located in the southern Tibetan Plateau, and is separated from the Qiangtang terrane to the north by the Bangong–Nujiang suture zone (BNSZ) and the Himalaya terrane to the south by the Indus–Yarlung suture zone (IYZS; Fig. 1). Based on marked differences in both the basement geology and sedimentary cover sequences, the Lhasa terrane can further be subdivided into the northern, central and southern sub-terranes, which are separated by the Shiquan River-Nam Tso mélange (SNMZ) and the Luobadui–Milashan fault (LMF; Fig. 2; Pan et al., 2004; Zhu et al., 2011, 2013), respectively.

Cambrian crystalline basement is exposed in the southern Lhasa terrane, it is represented by the Nyingchi Group that mainly consists of gneiss, amphibolite, schist and marble (Dong et al., 2010). Its Late Triassic-Cretaceous cover consists of volcano-sedimentary strata including sandstone, dacite, limestone and mudstone (Pan et al., 2004; Zhu et al., 2008, 2013), while middle to late Paleozoic sedimentary units are scarce (Fig. 3). The meso-Cenozoic magmatic belt in the southern Lhasa terrane is known as the Gangdese batholith. It was formed during the northward subduction of the NeoTethys oceanic slab and the subsequent India-Asia collision (Yin and Harrison, 2000; Ding et al., 2014; Zhu et al., 2019). The Gangdese batholith is mainly composed of Mesozoic granites, hornblende gabbros, granodiorites and tonalites, and Eocene to Neogene calc-alkaline and shoshonitic rocks (Ji et al., 2009; Zhu et al., 2015). The Linzizong volcanic succession formed around 69–43 Ma ago, unconformably overlying the strongly deformed Cretaceous strata in the south and central Lhasa terranes. Its rocks are of andesitic to rhyolitic composition and occur mainly as lava flows, pyroclastics and ignimbrites. This magmatic system probably resulted from the rollback and break-off of the subducting Indian slab (Pan et al., 2004; Mo et al., 2008; Lee et al., 2009). The northern Lhasa terrane is dominantly composed of Middle Triassic to Cretaceous sedimentary strata, including slates and sandstones with radiolarian (Pan et al., 2004; Nimaciren et al., 2005). The Mesozoic magmatic rocks mainly contain Early Cretaceous volcanic rocks and contemporaneous granitoids (Zhao et al., 2008; Zhu et al., 2009). The central Lhasa terrane has a Precambrian basement that is covered by very low-grade Permo-Carboniferous meta-sediments and Early Cretaceous volcano-sedimentary rocks (Fig. 3; Zhu et al., 2011; Zhang et al., 2012). They were intruded by Mesozoic and Cenozoic plutonic rocks (Fig. 3; Pan et al., 2004; Zhu et al., 2008, 2013). The Linzizong succession is mainly exposed in the western part of this sub-terrane, with limited outcrops in the north of the Linzhou basin (Pan et al., 2004; Mo et al., 2008).

The structural architecture of the Lhasa terrane is characterized by a number of major structures. The SNMZ extends ~SE–NW for ~2000 km in the northern part of the Lhasa terrane and probably represents an Early Cretaceous collision zone between the Qiangtang and northern Lhasa terranes (Fig. 2; Zhu et al., 2011, 2013). The LMF is a ~1500 km long thrust fault, representing a Carboniferous-Permian suture zone in the southern part of the Lhasa terrane (Fig. 2; Zhu et al., 2013). About 15 km south of the LMF, the local north-dipping Gulu-Hamu thrust cuts the Linzizong Group, positioning Triassic and Jurassic strata in its hanging wall

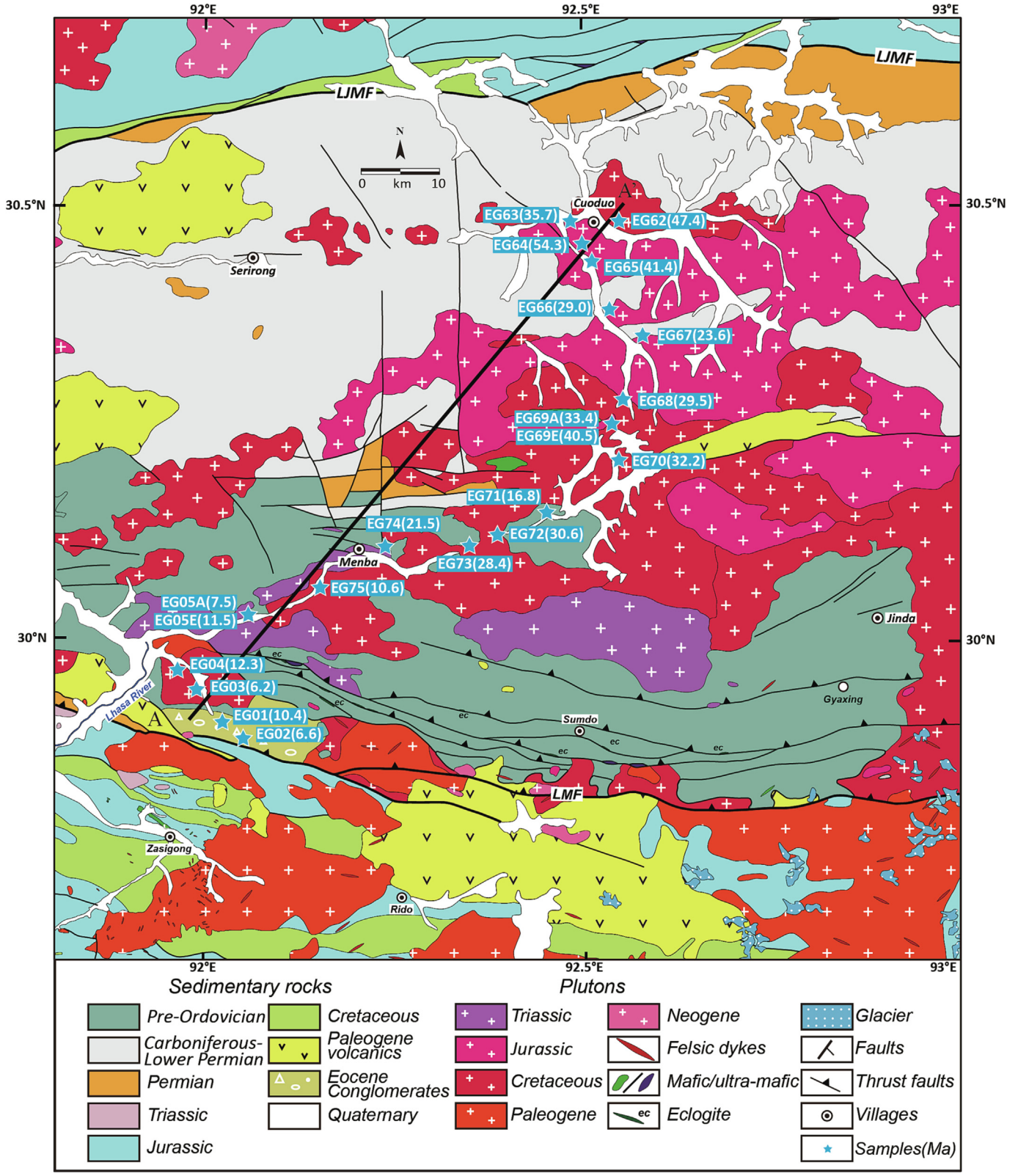


**Fig. 3.** Detailed geological map of the study area in the eastern part of the Lhasa terrane (modified from Yang, 2004; Li and Pan, 2011) with indication of our sample sites (numbers between brackets represent their AFT ages, expressed in Ma). The black line (A-A') represents the profile in Supplementary Data Fig. S1.

and the Linzizong Group in its footwall (He et al., 2007; Zhu et al., 2013). Its eastern end merges with the LMF (Li and Pan, 2011). The activity of the Gulu–Hamu thrust was limited to ~47–12 Ma based on (1) crosscutting relationships with the Linzizong Group; and (2) K-feldspar $^{40}Ar/^{39}Ar$ and AHe ages from the Qianggeren granite in the hanging wall of this thrust (Fig. 2; He et al., 2007; Ingalls

et al., 2018). The Great Counter thrust (GCT) and the Gangdese thrust (GT) are located in the southernmost Lhasa terrane (Fig. 2). The former is a south-dipping thrust system, juxtaposing the Tethyan Himalayan strata, ophiolitic mélange and the Xigaze basin (Murphy and Yin, 2003; Laskowski et al., 2018). Field and isotopic evidence indicates that this structure was active between ~23 and ~17 Ma (Yin et al., 1999; Harrison et al., 2000; Laskowski et al., 2017). The latter is a crustal-scale north-dipping thrust structure, and was active at ~27–17 Ma as determined by Ar-Ar thermochronology and structural relationships with the Kailas Conglomerate (Yin et al., 1994, 1999; Laskowski et al., 2018). The extension of the GT is still debated, Yin et al. (1994, 1999) suggested that it extends a long distance from the west of Xigaze city to the east of Zedang county (~84.5°E to ~93°E). Other researchers argue that this fault is buried by the Xigaze basin and the Tethyan sequences to the west of Lhasa city (Aitchison et al., 2003; Guo et al., 2018; Laskowski et al., 2018). In addition to these ~E–W-striking structures, several prominent ~N—S trending rifts are also developed in the southern Tibetan Plateau, including the Lunggar, Nyainqentanglha and Woka–Cuona rifts. Their evolution was related to the Miocene ~E–W orogenic collapse and extension in the Tibetan Plateau (e.g., Harrison et al., 1995; Styron et al., 2013; Bian et al., 2020).

## 3. Sample description and analytical methods

### 3.1. Sample information

All the samples were collected from the eastern part of the central Lhasa terrane, which geographically forms part of the external drainage area. Sixteen samples were taken from Late Triassic-Cretaceous granitic rocks, three sedimentary rocks were collected from pre-Ordovician and Carboniferous strata, and two conglomerates are from the late Eocene-Miocene Dazhuka Formation. The conglomerates were analyzed for AFT as whole rock, including both the matrix and clasts. Except for samples EG01-05E and EG75 that are near the Lhasa River and in the hanging wall of the LMF, other samples were collected away from major faults and river valleys (Figs. 2 and 3). Sample details including lithology, crystallization or stratigraphic ages, and locations are presented in Table 1.

### 3.2. Apatite fission track (AFT) thermochronology

The AFT method is based on the spontaneous fission decay of the $^{238}U$ isotope. Fission tracks (FTs) are linear lattice damages caused by $^{238}U$ fission in the apatite crystal lattice, and can be analyzed under an optical microscope after chemical etching by nitric acid. The surface density of etched FTs in apatite is a measure for the AFT age, which is a cooling age through the characteristic temperature window (e.g., Wagner and Van den haute, 1992). Between ~60–120 °C, FTs in apatite are partially annealed and shorten; this temperature range is defined as the apatite partial annealing zone (APAZ; e.g., Green et al., 1989; Wagner and Van den haute, 1992). At temperatures below ~60 °C FTs in apatite are considered (quasi) stable, while at elevated temperatures above ~120 °C, they anneal completely and rapidly on geological timescales. Contrary to etched surface tracks (used for determining the areal track density), some tracks occur completely below the observational surface and can be etched as well (through another surface track for example). These are called confined tracks and their etchable length will become shorter at elevated temperatures. These can thus be used as thermal history indicators (Gleadow et al., 1986). AFT ages combined with confined track length distributions can be used to model the thermal history of the samples through the APAZ, corresponding to ~2–4 km crustal depth (Ketcham, 2005; Ketcham et al., 2007).

In this work, the apatite grains were embedded in epoxy to be grinded and polished. The mounts were analyzed using the external detector method (EDM; Gleadow and Lovering, 1977). Spontaneous tracks in apatite were etched with a 5.5 M $HNO_3$ solution for 20 s at 21 °C, induced tracks in the muscovite ED with 40 % HF for 40 min at 20 °C. Irradiation was performed at the well-thermalized channel X26 of the BR1 nuclear reactor at the Belgian Nuclear Research Center (De Grave et al., 2010). Conventional ζ-ages were used to report the AFT ages (Hurford and Green, 1983; Hurford, 1990), with an overall weighted mean zeta of 338.0 ± 3.7 a·cm$^2$ (analyst W. Su), based on multiple Durango and Fish Canyon Tuff apatite age standards (Dazé et al., 2003; McDowell et al., 2005) and the IRMM-540 dosimeter glass (De Corte et al., 1998). The AFT analyses were performed using 2000× magnification on a Nikon Eclipse Ni-E microscope, with a DS-Ri2 camera and the Nikon TrackFlow system (Van Ranst et al., 2020a). More details on the analytical protocol used can be found in Nachtergaele

**Table 1**
Sample locations and lithology details.

| Sample | Lithology | GPS | | Elevation | Crystallization or stratigraphic age |
|---|---|---|---|---|---|
| | | N | E | (m) | |
| EG01 | Sandstone | 29°54′11.91″ | 91°59′02.88″ | 4158 | E3-N1; Yang, 2004 |
| EG02 | Conglomerate | 29°53′14.60″ | 92°00′23.48″ | 4221 | E3-N1; Yang, 2004 |
| EG03 | Biotite granite | 29°56′01.25″ | 91°57′40.50″ | 4048 | 195 Ma; Wang et al., 2017a |
| EG04 | K-feldspar granite | 29°58′33.61″ | 91°55′21.15″ | 3926 | 195 Ma; Zhu et al., 2011 |
| EG05A | Biotite granite | 30°01′11.76″ | 92°02′57.44″ | 4024 | 201 Ma; Li et al., 2016 |
| EG05E | Granodiorite | 30°01′11.76″ | 92°02′57.44″ | 4024 | 201 Ma; Li et al., 2016 |
| EG62 | Biotite granite | 30°28′16.81″ | 92°32′45.57″ | 4695 | K1; Yang, 2004 |
| EG63 | Sandstone | 30°28′46.80″ | 92°28′20.95″ | 4622 | *C2-P1*; Yang, 2004 |
| EG64 | Biotite granite | 30°27′07.53″ | 92°29′22.66″ | 4679 | J3; Yang, 2004 |
| EG65 | Biotite granite | 30°25′50.90″ | 92°29′55.61″ | 4748 | J3; Yang, 2004 |
| EG66 | Biotite granite | 30°22′38.01″ | 92°31′29.04″ | 4806 | J3; Yang, 2004 |
| EG67 | Biotite granite | 30°20′45.49″ | 92°33′59.34″ | 4873 | J3; Yang, 2004 |
| EG68 | Biotite granite | 30°16′12.41″ | 92°32′46.69″ | 5008 | 153 Ma; Zhu et al., 2011 |
| EG69A | Diorite | 30°14′31.35″ | 92°31′37.68″ | 5062 | 154 Ma; Zhu et al., 2011 |
| EG69E | Granite | 30°14′31.35″ | 92°31′37.68″ | 5066 | 154 Ma; Zhu et al., 2011 |
| EG70 | Sandstone | 30°11′53.23″ | 92°32′19.20″ | 4971 | Pre-Ordovician; Yang, 2004 |
| EG71 | Schist | 30°08′32.94″ | 92°27′02.88″ | 4777 | Pre-Ordovician; Yang, 2004 |
| EG72 | Biotite granite | 30°06′39.44″ | 92°22′43.50″ | 4621 | 154 Ma; Zhu et al., 2011 |
| EG73 | Biotite granite | 30°06′08.11″ | 92°20′23.97″ | 4437 | 154 Ma; Zhu et al., 2011 |
| EG74 | Biotite granite | 30°06′03.16″ | 92°13′41.29″ | 4244 | 210 Ma; Zhu et al., 2011 |
| EG75 | Granite | 30°03′30.45″ | 92°08′37.85″ | 4124 | 84 Ma; Meng et al., 2014 |

et al. (2018), Van Ranst et al. (2020b) and He et al. (2022). Not all the dated samples yielded sufficient quantity of measurable confined tracks due to their young AFT ages and/or low U concentrations. To increase the numbers of measurable confined tracks (i.e., tracks-in-track), 11 duplicate sample mounts were made and irradiated with $^{252}$Cf fission fragments (Donelick and Miller, 1991) at The University of Adelaide (Table 2).

### 3.3. Thermal history modeling

All aforementioned 11 samples yielded sufficient numbers of measurable confined tracks (>60) after $^{252}$Cf irradiation and were used for Markov Chain Monte Carlo inverse modeling performed by the QTQt software (Gallagher et al., 2009; Gallagher, 2012). Track density data and length-frequency distributions are the main inputs in the modeling software. We used the Ketcham et al. (2007) annealing equations and kinetic parameter $D_{par}$ (Donelick et al., 2005) for inverse modeling. The samples taken from a same plutonic massif were modeled together, (e.g., EG64/65, EG66/67, and EG68/72). We also integrated published zircon U-Pb ages as high-temperature constraints in the models. The prior time was set to the oldest age ± oldest age, and the prior for temperature is defined as 70 ± 70 ℃. The present surface temperature was set as 10 ± 10 ℃. For each modeling run we first set a burn-in of 10,000 iterations and a post-burn-in of 50,000 iterations to find the appropriate search parameters, after that 100,000 burn-in and 200,000 post-burn-in iterations were run.

## 4. Results

### 4.1. AFT age and length data

A total of twenty-one new AFT ages are obtained in this study. The mean zeta-ages ($t(\zeta)$) are used in the following discussion (Fig. 3; Supplementary Data Fig. S1; Table 2), their central ages are calculated as well. Radial plots for each sample are presented in Supplementary Data Fig. S2. All the samples passed the homogeneity test ($P(\chi^2)$ > 5 %), indicating single age populations (Galbraith, 1981; Green et al., 1989). Seven samples from near the Lhasa River, in the hanging wall of the LMF, including sandstone (EG01), conglomerate (EG02), and plutonic rocks (EG03-05E and EG75), show the youngest AFT ages that range from middle to late Miocene (~12 to ~6.2 Ma). In contrast, other samples that were collected away from the Lhasa River and LMF show older AFT ages (Fig. 3). Three pre-Permian sedimentary rocks (EG63, 70–71) yield late Eocene to middle Miocene AFT ages between ~36 to ~17 Ma, which are much younger than their depositional ages, indicating that the AFT clocks in these sedimentary rocks have been reset. The other 11 plutonic rocks whose crystallization ages range from ~201 to ~84 Ma, yield AFT cooling ages from ~54 to ~22 Ma (Tables 1 and 2). Except for those samples whose apparent AFT ages are younger than ~15 Ma, the ages exhibit a linear relationship with elevation (older at higher elevation) and latitude (older to the north) (Fig. 5 and Supplementary Data Fig. S1). The mean track lengths (MTL) of samples with old AFT ages (>41 Ma; EG62, 64 and 65) are ~12.8–12.5 μm, which are generally shorter than those (~13.6 to ~12.8 μm) of the youngest samples (<13 Ma; EG03, 05A and 75). The other 4 samples (EG66, 67,78 and 74) have a wide range of MTLs, ranging from ~13.1 to ~11.4 μm (Table 2; Supplementary Data Fig. S3).

### 4.2. Thermal history modeling results

Detailed *t-T* paths and length distribution histograms for each modeled samples are shown in Supplementary Data Fig. S3, their expected thermal history curves are compiled in Fig. 4b. For a more quantitative description of the cooling history, we empirically define the cooling rates of ~5–10 ℃/Ma and >10 ℃/Ma as moderate and rapid cooling, respectively (e.g., Su et al., 2022).

**Table 2**
Apatite fission track data.

| Sample | No. of Grains | Spontaneous | | Induced | | Dosimeter | | $P(\chi^2)$ (%) | Dispersion (%) | $\rho_s/\rho_i$ | Zeta ($\zeta$) age (Ma ± 1 s. e.) | | Central age (Ma ± 1 s. e.) | | Track length and $D_{par}$ | | | |
|---|---|---|---|---|---|---|---|---|---|---|---|---|---|---|---|---|---|---|
| | | $N_s$ | $\rho_s$ (cm$^{-2}$) | $N_i$ | $\rho_i$ (cm$^{-2}$) | $N_d$ | $\rho_d$ (cm$^{-2}$) | | | | | | | | $N_l$ | MTL (μm) | Length range (μm) | $D_{par}$ (μm) |
| EG01 | 45 | 50 | 0.257 | 483 | 2.558 | 2708 | 541,520 | 96.94 | 0.00 | 0.114 | 10.4 | 1.6 | 9.5 | 1.4 | / | / | / | / |
| EG02 | 52 | 28 | 0.068 | 390 | 1.050 | 2798 | 559,592 | 99.16 | 0.00 | 0.070 | 6.6 | 1.3 | 6.8 | 1.3 | / | / | / | / |
| EG03 | 18 | 21 | 0.261 | 394 | 5.004 | 2803 | 560,515 | 42.81 | 2.76 | 0.066 | 6.2 | 1.4 | 5.1 | 1.1 | 81 | 13.2 | 9.5–15.6 | 2.27 |
| EG04 | 26 | 36 | 0.476 | 336 | 3.973 | 2807 | 561,485 | 89.06 | 0.00 | 0.129 | 12.3 | 2.2 | 10.2 | 1.8 | / | / | / | / |
| EG05A | 27 | 85 | 0.457 | 1107 | 5.807 | 2711 | 542,217 | 99.12 | 0.00 | 0.082 | 7.5 | 0.9 | 7.0 | 0.8 | / | / | / | / |
| EG05E | 27 | 61 | 0.262 | 565 | 2.428 | 2812 | 562,408 | 86.27 | 0.00 | 0.121 | 11.5 | 1.6 | 10.3 | 1.4 | 75 | 13.6 | 8.4–16.0 | 1.60 |
| EG62 | 15 | 1276 | 8.889 | 2574 | 17.827 | 2817 | 563,330 | 82.43 | 0.01 | 0.500 | 47.4 | 1.9 | 47.0 | 1.9 | 101 | 12.5 | 9.7–15.4 | 1.38 |
| EG63 | 41 | 1294 | 7.666 | 3606 | 21.186 | 2821 | 564,161 | 68.19 | 2.18 | 0.375 | 35.7 | 1.4 | 34.1 | 1.3 | / | / | / | / |
| EG64 | 22 | 2165 | 11.143 | 3802 | 19.695 | 2825 | 565,084 | 41.57 | 2.08 | 0.571 | 54.3 | 1.9 | 54.2 | 1.9 | 102 | 12.8 | 8.9–16.1 | 1.44 |
| EG65 | 18 | 1171 | 7.324 | 2734 | 17.048 | 2830 | 566,053 | 32.72 | 2.53 | 0.434 | 41.4 | 1.7 | 40.9 | 1.7 | 101 | 12.8 | 9.1–15.0 | 1.45 |
| EG66 | 13 | 164 | 2.170 | 543 | 7.263 | 2835 | 566,976 | 98.7 | 0.00 | 0.303 | 29.0 | 2.7 | 28.9 | 2.7 | 102 | 13.1 | 9.4–16.0 | 1.48 |
| EG67 | 26 | 272 | 1.287 | 272 | 5.294 | 2839 | 567,899 | 46.63 | 3.59 | 0.246 | 23.6 | 1.7 | 23.0 | 1.6 | 102 | 12.3 | 8.2–15.8 | 1.50 |
| EG68 | 16 | 423 | 4.096 | 1378 | 13.402 | 2844 | 568,822 | 99.51 | 0.00 | 0.308 | 29.5 | 1.8 | 29.4 | 1.8 | 103 | 12.5 | 10.1–15.3 | 1.39 |
| EG69A | 29 | 45 | 0.386 | 133 | 1.146 | 2856 | 571,176 | 99.41 | 0.00 | 0.347 | 33.4 | 5.8 | 32.6 | 5.7 | / | / | / | / |
| EG69E | 25 | 237 | 2.067 | 634 | 5.278 | 2860 | 572,053 | 42.9 | 4.80 | 0.420 | 40.5 | 3.2 | 36.1 | 2.9 | / | / | / | / |
| EG70 | 19 | 128 | 2.090 | 378 | 6.330 | 2865 | 572,976 | 97.42 | 0.00 | 0.333 | 32.2 | 3.4 | 32.7 | 3.4 | / | / | / | / |
| EG71 | 17 | 87 | 1.855 | 431 | 9.095 | 2869 | 573,899 | 90.34 | 0.00 | 0.174 | 16.8 | 2.0 | 19.4 | 2.3 | / | / | / | / |
| EG72 | 18 | 206 | 1.785 | 692 | 6.147 | 2875 | 574,914 | 89.38 | 0.00 | 0.315 | 30.6 | 2.5 | 28.9 | 2.4 | 100 | 13 | 10.1–15.8 | 1.62 |
| EG73 | 27 | 239 | 1.180 | 858 | 4.187 | 2879 | 575,837 | 85.23 | 0.02 | 0.292 | 28.4 | 2.2 | 27.1 | 2.1 | / | / | / | / |
| EG74 | 29 | 259 | 1.202 | 1228 | 5.566 | 2884 | 576,760 | 91.67 | 0.02 | 0.221 | 21.5 | 1.5 | 20.5 | 1.5 | 87 | 11.4 | 8.0–15.6 | 1.45 |
| EG75 | 23 | 204 | 0.784 | 1882 | 7.249 | 2888 | 577,683 | 89.72 | 0.00 | 0.109 | 10.6 | 0.8 | 10.6 | 0.8 | 66 | 12.8 | 9.7–15.5 | 1.39 |

$N_s$, $N_i$ and $N_d$ are the number of counted spontaneous tracks (in the apatite), induced tracks (in the muscovite external detector, ED) and induced tracks in the ED irradiated against regularly spaced Uranium-doped glass dosimeters (IRMM-540) in the irradiation package, respectively. $\rho_s$, $\rho_i$ and $\rho_d$ represent the density of spontaneous tracks (in the apatite), induced tracks (in the ED) and induced tracks from the glass dosimeters, respectively. $P(\chi^2)$ is the chi-squared probability that the dated grains have a constant $\rho_s/\rho_i$ ratio (Galbraith, 1981). An $\zeta$-value of 338.0 ± 3.7 a·cm$^2$ was used (Analyst W. Su) for the calculation of the AFT zeta ages. The AFT central ages were calculated using the RadialPlotter software (Vermeesch, 2009). The number of measured lengths ($N_l$), mean track lengths (MTL), length ranges are obtained by measuring a number of natural, horizontal confined tracks. All the obtained confined tracks benefited from $^{252}$Cf irradiation.

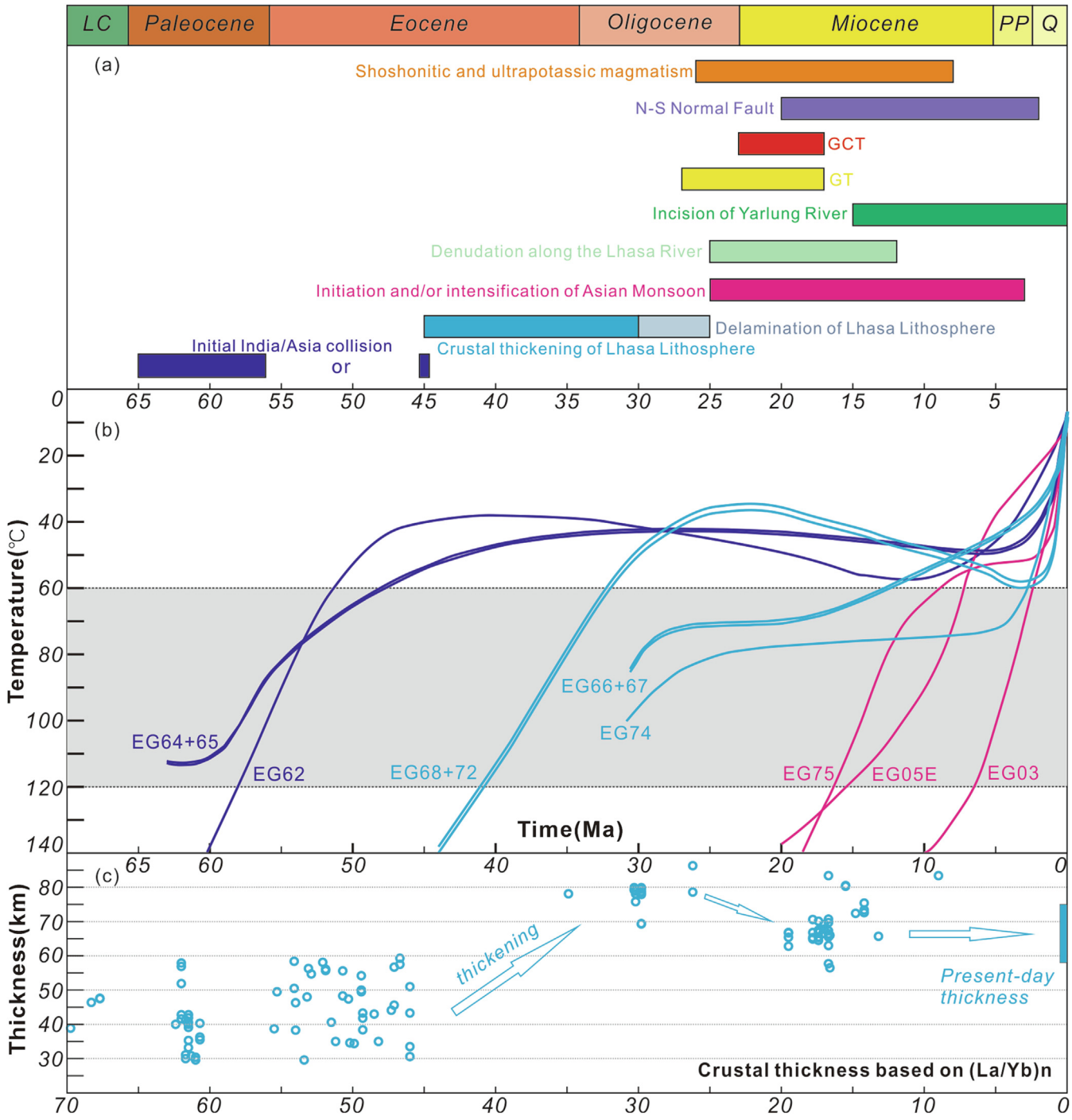


**Fig. 4.** (a) Timescale of major geologic and climatic events in the southern Tibetan Plateau: shoshonitic and ultrapotassic magmatism (Chung et al., 2005; Zhao et al., 2009); activities of the N–S normal faults and rift systems (Sundell et al., 2013; Wolff et al., 2019; Zhang et al., 2020); activity of the Great Counter thrust (GCT, Laskowski et al., 2018); motion along the Gangdese thrust (GT, Yin et al., 1994, 1999; Harrison et al., 2000; Murphy and Yin, 2003); incision of the Yarlung River (Dai et al., 2021); fast denudation along the Lhasa River (Cai et al., 2021); initiation and intensification of the Asian monsoon (Sun and Wang, 2005; Sanyal et al., 2010); crustal thickening of the Lhasa lithosphere (Zhu et al., 2017; Tang et al., 2020); delamination of the Lhasa lithospheric mantle (Chung et al., 2003; Zhao et al., 2009); initial India-Asia collision (Hu et al., 2016a; Kapp and Decelles, 2019; Ding et al., 2022). (b) Compilation of all our thermal history models (expected models) from the central Lhasa terrane. (c) Crustal thickness of the Lhasa terrane based on whole-rock $(La/Yb)_n$ ratio (Zhu et al., 2017; Cao et al., 2020). Present-day crustal thickness is calculated by using the CRUST 1.0 model (Laske et al., 2013).

Our samples can be divided into three groups based on differences in AFT ages and thermal histories (Fig. 4b; Table 2). The first group is represented by samples EG62, 64 and 65 that exhibit the oldest AFT apparent ages. Cooling path of sample EG62 enters the APAZ in the latest Paleocene (~58 Ma), with fast cooling occurring between ~58–52 Ma (Fig. 4b). A 'reheating' event is indicated to have existed in the later stage, but this time–temperature curve is beyond the APAZ and the sensitivity limit of the AFT system, and thus will not be discussed. This (early Cenozoic) cooling phase is also revealed by samples EG64 and 65, their joint model shows a moderate cooling between ~60 and ~48 Ma (Fig. 4b). The second group is composed of samples EG66-68, 72 and 74. The joint inver-

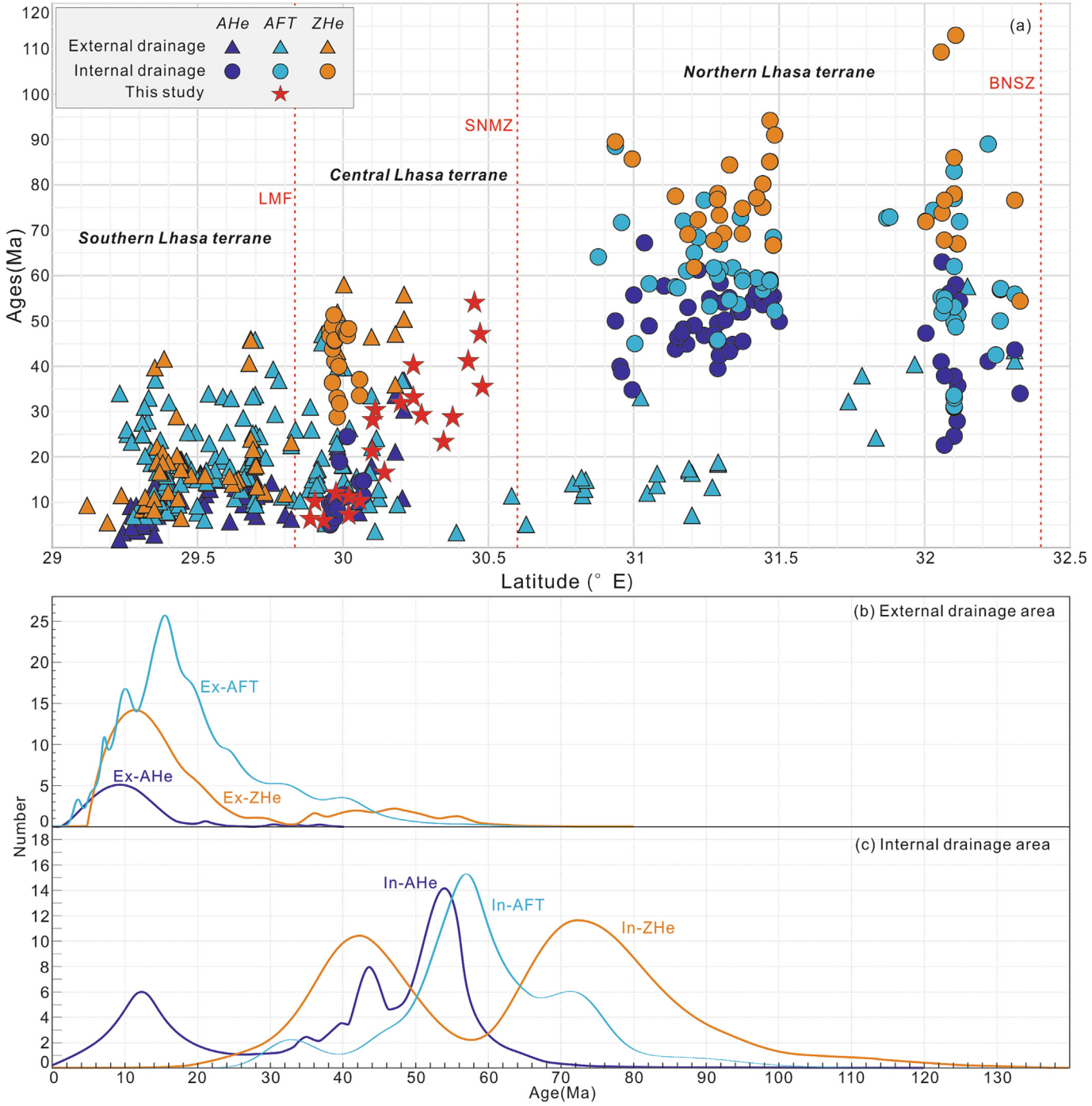


**Fig. 5.** (a) Compilation of the low-temperature thermochronological data (AHe, AFT and ZHe) available from the Lhasa terrane (data from the Namche-Barwa were not used here). The approximate locations of faults are marked along 92°E in Fig. 2. Abbreviations are as in Figs. 1 and 2. (b) and (c) Probability density plots of the low-temperature thermochronological data in the external drainage area and internal drainage area of the southern Tibetan Plateau, respectively. The compiled dataset can be found in Supplementary Data Table S1.

sion of EG68 and 72 indicates a moderate cooling between ~40–32 Ma (Fig. 4b). While the joint modeling of EG66 and 67 starts from a relatively low-temperature state and indicates a younger moderated cooling phase around ~31–28 Ma, followed by slow cooling rates until ~18 Ma (Fig. 4b). Sample EG74 shows a similar cooling curve to the joint model of EG66 and 67, and a moderate cooling during the early Oligocene with subsequent slow cooling since the late Oligocene (Fig. 4b). The third group contains the remaining three samples EG03, 05E and 75, whose cooling curves pass through the APAZ during ~16–4 Ma with moderate to fast cooling rates during the middle Miocene-early Pliocene (Fig. 4b).

## 5. Discussion

### 5.1. Cenozoic thermal-tectonic evolution of the eastern Lhasa terrane

The samples taken close to the Lhasa River and the Luobadui-Milashan (LMF), in the southern part of the central Lhasa terrane

(EG01-05E and EG75; Fig. 3), have relatively young AFT ages (~12.3–6.2 Ma; Fig. 4b; Table 2). The other samples further away from river valleys and faults (in the central and northern parts of the central Lhasa terrane), have comparably older AFT ages (~54.3–21.5 Ma; Fig. 3), recording cooling and exhumation information of the eastern segment of the central Lhasa terrane without the influence of river incision and fault activity. Based on the acquired thermal history models, three enhanced cooling phases during the Cenozoic can be recognized: (i) the Paleocene-early Eocene (~60–48 Ma); (ii) the late Eocene to early Oligocene (~40–28 Ma); and (iii) the middle Miocene-early Pliocene (~16–4 Ma; Fig. 4b). For a more comprehensive understanding of the thermal history of the Lhasa terrane, we compiled previously published low-temperature thermochronological (LTT) data (i.e., ZHe, AFT and AHe) in the Lhasa and southern Qiangtang terranes. These data can in first order be subdivided into two groups based on their location (i.e., external or internal drainage area) (Figs. 1, 2 and 5). In the external drainage area (southern Tibetan Plateau), all the LTT ages are younger than ~60 Ma, and the majority of them are younger than ~25 Ma (Fig. 5b). Compared to the data in other places of the external drainage area, particularly regarding the AFT ages, our samples yield several AFT ages that are older than ~40 Ma and a large set of ~40–20 Ma AFT ages. The latter are similar to the other data pertaining to the external drainage area (Fig. 5).

*5.1.1. Paleocene-early Eocene (~60–48 Ma)*

In the northernmost sampling profile, several granitic samples recorded Paleocene-early Eocene accelerated cooling in the central Lhasa terrane (~60–48 Ma; Figs. 3 and 4b). The published LTT data show that the northern Lhasa terrane experienced accelerated cooling phases mainly during the Late Cretaceous to middle Eocene (~80–45 Ma; Hetzel et al., 2011; Rohrmann et al., 2012; Haider et al., 2013), much earlier than those of the central and southern Lhasa terranes (Fig. 5). The NeoTethys oceanic lithosphere underwent long-lasting northward subduction, which probably initiated between ~240 and ~190 Ma and consumed thoroughly when the India plate collided with Asia continent (Ji et al., 2009; Wang et al., 2016). Although there is no agreement on the onset of India-Asia initial collision, which was considered to have occurred between ~60 and ~45 Ma (e.g., Hu et al., 2016a; Kapp and Decelles, 2019; Ding et al., 2022), some other geological records are much clearer. At ~70 Ma, the convergence rate between India and Asia plates accelerated to>120 mm/yr (van Hinsbergen et al., 2011; Cande and Patriat, 2015; Gibbons et al., 2015). The northward subduction of the NeoTethys oceanic lithosphere produced massive ~70–50 Ma magma that intruded the Gangdese arc, such as the widespread Linzizong volcanic succession (Mo et al., 2008; Lee et al., 2009). This is also accompanied by crustal shortening of the Gangdese retroarc thrust belts (Kapp et al., 2003, 2007) and thickening of the Gangdese arc. The crustal thickness of the southern Lhasa terrane was ~37 km at ~70 Ma and thickened to ~58–50 km during ~55–45 Ma (Fig. 4c; Zhu et al., 2017; Tang et al., 2020). The crustal thickening could have led to the formation of a high-elevation "Lhasaplano" (Kapp et al., 2007). For instance, the Linzhou basin in the southern Lhasa terrane achieved a >4100 m elevation in ca. 58–47 Ma as documented by the stable isotope evidence (Ding et al., 2014; Ingalls et al., 2018). The elevated Lhasa terrane was actively being eroded and provided detrital sediments to the retro-arc foreland basin (Kapp et al., 2007) and forearc basins along the Indus-Yarlung suture zone (Ding et al., 2005; Wang et al., 2012; DeCelles et al., 2014; Hu et al., 2016b). Consequently, we suggest that the Paleocene-early Eocene basement cooling recognized in the study area was possibly linked to denudation of the thickened crust as response to the accelerated northward subduction of the NeoTethys oceanic lithosphere.

*5.1.2. Late Eocene to early Oligocene (~40–28 Ma)*

The late Eocene to early Oligocene cooling event (~40–28 Ma) is recorded by samples along the Menba – Cuoduo, and are not near important river valleys or local tectonic structures (Figs. 3 and 4b). In the external drainage area, this cooling phase is also recognized in the northern Lhasa terrane (e.g., Anduo granitoids; Wang et al., 2007; Li et al., 2019), the central part of the southern Lhasa terrane (e.g., Qianggeren granite; Ge et al., 2017; Huang et al., 2022), and the eastern part of the central Lhasa terrane (e.g., the Sharang porphyry Mo deposit and Yaguila skarn Pb-Zn-Ag deposit; Zhao et al., 2015). The driving force for late Eocene-early Oligocene regional basement cooling is diverse. This cooling event in the southern Lhasa terrane was likely to have been triggered by crustal thickening (Ge et al., 2017). Whereas the cooling occurring in the Qianggeren granite is considered to be localized and resulting from the movement of the Gulu-Hamu thrust (He et al., 2007; Huang et al., 2022). In this study, samples with late Eocene to early Oligocene AFT ages are distant from faults and large rivers valleys as mentioned above (Fig. 3), thus this cooling event probably was not induced by local fault activity or enhanced river incision, but related to near-surface exhumation after crustal thickening of the Lhasa lithosphere. During the late Eocene to early Oligocene (~45–30 Ma), the igneous activity that produced the Gangdese batholith over time gradually halted after the break-off of the Neo-Tethys slab. Moreover, the continuous northward indentation of the India plate into Eurasia caused significant contraction in the Lhasa lithosphere and resulted in its thickening (Chung et al., 2005, 2009; Zhu et al., 2015). The crustal thickening is demonstrated by the calculation of whole-rock La/Yb ratios of intermediate intrusive rocks and Nd isotopes in the Gangdese batholith, which indicates that the crust was ~58–50 km at ~45 Ma and then thickened to over 70 km around 30 Ma (Fig. 4c; Zhu et al., 2017; DePaolo et al., 2019). After this crustal thickening and tectonic uplift, relief developed and surface erosion followed. We hence propose that the late Eocene-early Oligocene basement cooling in the central Lhasa terrane was probably connected with coeval crustal thickening and consequential erosion. Considering that the precise time of (initial) India-Asia collision is still controversial (Hu et al., 2016a; Kapp and Decelles, 2019; Ding et al., 2022), it cannot be solely determined by the results in this study whether this crustal thickening process was induced by the India-Asia collision.

*5.1.3. Middle Miocene-early Pliocene (~16–4 Ma)*

The latest rapid cooling event identified in our study area is revealed by samples EG01-05E and EG75, and it took place during the middle Miocene to early Pliocene (~16–4 Ma; Fig. 4b). Samples EG01 and 02 are from the Dazhuka Formation conglomerates, whose depositional age is roughly constrained to the late Eocene-early Miocene, and is considered an analogue of the coeval Liuqu Conglomerate in the Indus-Yarlung suture zone (Li et al., 2015a). The AFT ages of these two samples are ~10.4 and ~6.6 Ma, respectively, younger than their envisaged depositional age (Table 2). Some analyzed apatite grains display AFT ages that approximate their depositional age (Tables 1 and 2), indicating that their AFT systems were at least partially reset. Samples EG03-05E and EG75 are granitic rocks, their apparent AFT ages are ~12.3–6.2 Ma and the inverse modeling results define a middle Miocene-early Pliocene rapid cooling phase (Fig. 4b). All these aforementioned samples (EG01-05E and EG75) exhibit the youngest AFT ages from our data set, which are younger than those from downstream in the Lhasa River valley (Pan et al., 1993; Copeland et al., 1995; Li et al., 2016; Dai et al., 2021).

Our samples were collected near the midstream of the Lhasa River valley and in the hanging wall of the LMF, i.e., one of the major thrusts in the Gangdese retro-arc thrust belt (Figs. 2 and

3; Zhu et al., 2013; Kapp et al., 2007). The Gulu–Hamu thrust is situated at the northern edge of the Linzhou basin, its middle section (north of the Linzhou county) is located ~15 km south of the LMF, and its eastern end merges with the LMF (Fig. 2; He et al., 2007; Li and Pan, 2011). The Qianggeren granite was emplaced at ~52 Ma and is situated now in the hanging wall of the Gulu–Hamu thrust (He et al., 2007). It experienced rapid exhumation around 42–26 Ma and 15–12 Ma, respectively, based on ZHe and AHe data, probably as a consequence of movements along the Gulu–Hamu thrust (Ingalls et al., 2018; Huang et al., 2022). This implies that the Gulu–Hamu thrust was likely active around 47–12 Ma derived from these thermochronological data and the crosscutting relationship with the Qianggeren granite (Fig. 2; He et al., 2007; Ingalls et al., 2018). Considering the close temporal and spatial relationship between our sample sites, the AFT ages and the LMF (e.g., eastward extension of the Gulu–Hamu thrust), we suggest that the activity of the Gulu–Hamu thrust was an important triggering mechanism for the exhumation and hence cooling of these rocks.

In addition, the Asia monsoon intensified consecutively around ~15–13 Ma, ~8 Ma and ~3 Ma ago (Fig. 4a; Sun and Wang, 2005; Clift and Webb, 2018). This affected a large area of the Tibetan Plateau, including southern and southeastern Tibet, and the Himalaya orogen (Clark et al., 2005; Clift et al., 2008; Clift and Webb, 2018; Nie et al., 2018; Dai et al., 2021). The Yarlung River drainage experienced a two-stage (~15–9 Ma and ~5–2 Ma) accelerated incision due to the increased precipitation, causing accelerated rock denudation (Clift et al., 2008; Nie et al., 2018; Cai et al., 2021; Dai et al., 2021). Three samples (EG03, 05E and 75) near the Lhasa River (one of the main tributaries of the Yarlung River) show a contemporaneous middle Miocene-early Pliocene accelerated cooling period (Fig. 4a and b). Therefore, the enhanced incision of the Lhasa River due to intensification of the Asian monsoon was likely to be another mechanism causing this middle Miocene-early Pliocene cooling event. It is noted that rock samples which exhibit late Cenozoic AFT ages and cooling in their respective thermal history models may have also experienced the aforementioned earlier enhanced exhumation, as induced by regional tectonic events such as lithospheric delamination. However, these thermal signals have been removed by more recent erosion and exhumation.

### 5.2. Implications for relatively high-relief topography of the southern Tibetan Plateau external drainage area

The internal and external drainage areas in the southern Tibetan Plateau have contrasting relief. The former shows typical high-elevation low-relief topography, while for the latter, the topographic relief is relatively high, and a clear boundary exists between them (Fig. 1). Regarding the Lhasa terrane and the Himalaya, the LTT ages in the internal drainage area are generally older than those in the external drainage area (Fig. 5). The LTT ages in the internal drainage area are mainly clustered between the Late Cretaceous and early Eocene (Fig. 5a and c), whereas almost all the LTT data in the external drainage area are younger than 60 Ma and most even younger than ~25 Ma (Fig. 5a and b). Although LTT studies suggest that the interior plateau (the northern Lhasa terrane) has experienced intense uplift and exhumation during ~80–45 Ma (Hetzel et al., 2011; Rohrmann et al. 2012; Haider et al., 2013), it was still a topographic depression in the Paleogene, and did not reach its present elevation (>4 km) until ~29–26 Ma as revealed by paleoaltimetry evidence (Rowley and Currie, 2006; DeCelles et al., 2007; Fang et al., 2020; Xiong et al., 2022). The low-relief surface was established at the same time as the northern Lhasa terrane reached its high elevation (Han et al., 2019; Li et al., 2022; Xue et al., 2022). In contrast, the southern Lhasa terrane reached its present elevation (>4 km) around 58–47 Ma ago, much earlier than the northern Lhasa terrane (Ding et al., 2014; Ingalls et al., 2018). At present, the whole Lhasa terrane has almost identical elevation but contrasting relief characteristics (Fig. 1), which may have resulted from long-term effects from tectonic uplift, fault activity, river incision and climate change (Su et al., 2022). We here discuss the possible mechanisms that have led to the formation of this 'contrasting' relief.

During the latest Cretaceous-early Eocene, the largest difference of the southern Lhasa terrane and the northern Lhasa terrane is that they have different elevations as previously mentioned (Fig. 6a; Ding et al., 2022). During the late Eocene to early Oligocene (~40–30 Ma), the igneous activity in the southern Lhasa terrane halted because of the break-off of the NeoTethys slab. After that, the Lhasa lithosphere thickened due to the continuous northward indentation of the Indian plate (Chung et al., 2005, 2009; Zhu et al., 2015, 2017; DePaolo et al., 2019). The significant change in the Lhasa terrane is that the northern Lhasa terrane uplifted to the same elevation as the southern Lhasa terrane, and the low-relief landscape was developed as well (Fig. 6b; Han et al., 2019; Ding et al., 2022; Li et al., 2022; Xue et al., 2022). Since then, the northern Lhasa terrane has resided in an arid environment and experienced long-term tectonic quiescence. Thus, it makes sense that the >30 Ma LTT ages are widely preserved in the internal drainage area (Fig. 5; Han et al., 2019; Li et al., 2022; Xue et al., 2022).

The majority of the available LTT ages in the studied external drainage area are Miocene, significantly younger than those from the internal drainage area (Fig. 5a and b), implying that the external drainage area (i.e., eastern Lhasa terrane) experienced more recent crustal exhumation than the internal one. It is suggested that these more recent exhumation events were triggered by various mechanisms including tectonic uplift, river incision and climate change (e.g., Copeland et al., 1995; Dai et al., 2013; Tremblay et al., 2015; Li et al., 2016; Ge et al., 2017; Su et al., 2022). They may account for the development of relatively high-relief topography in the external drainage area. In the following we discuss these possible mechanisms chronologically.

During the latest Oligocene to middle Miocene, the southern Tibetan Plateau experienced intense magmatism and tectonic activity (Chung et al., 2005; Kapp and DeCelles, 2019). In the latest Oligocene (~26–23 Ma), the southward rollback of the Indian continental lithosphere and subsequent slab break-off caused a fast kinematic transition from extension to contraction along the Yarlung Zangbo suture zone, and coeval deposition of the Kailas Conglomerate (Fig. 6c; DeCelles et al., 2011; Leary et al., 2016). In this process, the Lhasa lithospheric root delaminated, resulting in the upwelling of hotter asthenosphere, producing massive shoshonitic-ultrapotassic magmatism (Chung et al., 2003, 2005,2009; Ji et al., 2009; Zhao et al., 2009; Kapp and Decelles, 2019). However, this magmatism mainly occurred in the southern Lhasa terrane and only rarely reached the central and northern Lhasa terranes (Kelly et al., 2020), owing to different crustal properties of these terranes (Lu et al., 2022). The crust of the southern Lhasa terrane represents homogeneous juvenile accreted material, while the central Lhasa terrane is characterized by relatively ancient crystalline basement (Lu et al., 2022). In addition, the subducted Indian continental lithosphere is not a homogeneous slab. It shows significant east–west lateral variations in its dip and geometry (Zhao et al., 2010). The Indian continental lithosphere appears to extend further north in central than in eastern Tibet. For example, it reaches ~350 km depth at ~31°N along 85°E but at ~30°N along 91°E (Liang et al., 2016). This corresponds to the internal drainage area in the west and external drainage area in the east, respectively (Figs. 1 and 6c).

Upper crustal tectonics also account for regional differences. In the southern Tibetan Plateau, the GT was active during the late Oligocene-early Miocene (~27–17), and the GCT between ~23 to

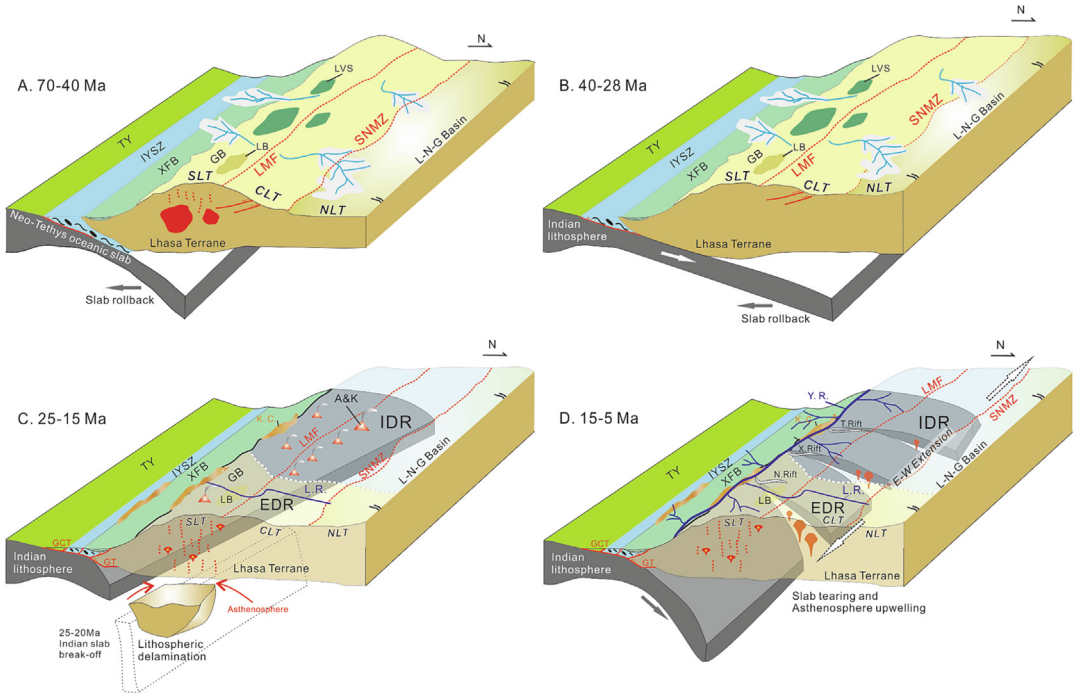


**Fig. 6.** Latest Cretaceous to late Miocene tectonic model for the Lhasa terrane (modified from Li et al., 2016). (a) ~70–40 Ma, the development of an Andean-type Gangdese Belt in the southern Lhasa terrane. (b) ~40–28 Ma, the crustal thickening in the Lhasa terrane; the northern Lhasa terrane was uplifted to its present elevations. (c) ~25–15 Ma, rollback and break-off of the subducted Indian slab; delamination of the southern Lhasa terrane lithospheric mantle with associated asthenosphere upwelling; activity of the Gangdese and Great Counter thrusts. (d) ~15–5 Ma, accelerated incision of the Yarlung River commenced in the southern Lhasa terrane; contemporaneous ~E-W extension and north-striking rift systems developed in southern Tibet. Refer to the text for detailed discussion. Abbreviations: A&K = adakitic, shoshonitic and ultrapotassic magmatism; CLT = central Lhasa terrane; EDR = External drainage area; GB = Gangdese batholith; GCT = Great Counter thrust; GT = Gangdese thrust; IDR = Internal drainage area; IYSZ = Indo-Yarlung suture zone; K.C. = Kailas Conglomerate; L-*N*-G Basin = Lunpola-Nima-Gaize Basin; L.R. = Lhasa River; LB = Linzhou basin; LMF = Luobadui-Milashan fault; LVS = Linzizong volcanic successions; N. Rift = Nyainqentanghla Rift; NLT = northern Lhasa terrane; SLT = southern Lhasa terrane; SNMZ = Shiquan River-Nam Tso mélange zone; T. Rift = Tangra Yum Rift; TY = Tethyan Himalaya; X. Rift = Xainza Rift; XFB = Xigaze Forearc Basin.

~17 Ma (Fig. 2; Yin et al., 1994, 1999; Harrison et al., 2000; Murphy and Yin, 2003; Laskowski et al., 2017, 2018). These two thrusts temporally overlapped, constituting a hinterland-dipping duplex that was controlled by subduction dynamics beneath the Gangdese magmatic arc (Fig. 6c; Laskowski et al., 2018). The single activity of the GT (Dai et al., 2013; Li et al., 2016; Ge et al., 2017) or the movement of this duplex (Laskowski et al., 2018; Taylor et al., 2021) may have caused the late Oligocene-middle Miocene (~25–15 Ma) accelerated exhumation of the Gangdese batholith. This period of basement cooling probably only occurred in the southern Lhasa terrane, and not in the central and northern Lhasa terranes, for almost no contemporaneous cooling ages have been documented there (Figs. 2 and 5b).

During the middle Miocene to late Miocene (~15–5 Ma), the India plate continued to subduct, producing smaller volumes of magma that progressively diminish northward in the Lhasa terrane (Chung et al., 2005; Kapp and DeCelles 2019; Kelly et al., 2020). During slab break-off, additional segmentation occurred along internal weak zones and heterogeneities. Low P- and S-wave velocities and magnetotelluric data show that the subducted Indian lithosphere beneath southern Tibet was fragmented into four pieces with differential subduction angles. The dip angle is steeper in the east as compared to the west (Chen et al., 2015; Liang et al., 2016; Wang et al., 2017b; Li and Song, 2018). This fragmentation or tearing of the slab with subsequent asthenospheric upwelling probably caused ~E-W orogen-parallel extension in the southern Tibet Plateau. This process formed a series of north-striking normal faults and associated rift structures in the northern Himalaya and Lhasa terranes (Chen et al., 2015; Li and Song, 2018; Bian et al., 2020, 2022). These were mainly active between ~23–3 Ma (e.g., Styron et al., 2013; Sundell et al., 2013; Li et al., 2015b; Kapp and DeCelles, 2019; Wolff et al., 2019; Bian et al., 2020). The majority of the LTT data in the southern Lhasa terrane coincide with this time-span (Figs. 2 and 5). Hence, the rift development possibly had an essential effect on basement exhumation and cooling of the eastern Lhasa terrane (Fig. 6d; Pan et al., 1993; Harrison et al., 1995; Dai et al., 2021).

River incision and climate conditions can have exerted additional influences on the regional topography. At present, the mean precipitation in the southern Tibetan Plateau and the Himalayas is more than ~1000 mm/a, much higher than that of the internal drainage area (<500 mm/a) which mainly occupies central and northern Tibet (Bookhagen et al., 2005; Maussion et al., 2014). Except for the difference in present precipitation, the internal drainage area has been in an arid climatic condition since the late Oligocene (~26 Ma), estimated by the evaporitic lacustrine and eolian dune-field deposits and their carbon and oxygen isotopic data (DeCelles et al., 2007). An arid environment is usually characterized by less intensive chemical weathering and surface erosion, which tends to facilitate the development of a low-relief topography (Fielding et al., 1994; Xue et al., 2022). Whereas in the external drainage areas, the environment is relatively humid and several large rivers developed, causing rapid incision of the southern and eastern Tibetan Plateau (Fig. 1; Liu-Zeng et al., 2018b; Nie et al., 2018; Dai et al., 2021). Taking the Yarlung River as an example, as the largest river in the southern Tibetan Plateau, it was formed by integration of several tributaries originating in the Gangdese Mountains and the Himalayas. Along the Xigaze–Gyacha section (Fig. 2), rapid exhumation along the Yarlung River main stream predominantly occurred in the mid-Miocene (~15–9 Ma) and Pliocene-Pleistocene (~5–2 Ma; Dai et al., 2021). The Lhasa and Nyingoh Rivers are two main tributaries of the Yarlung River.

Recent studies have demonstrated that the Lhasa River caused a two-stage rapid denudation along its trajectory around ~25–16 Ma and ~16–12 Ma (Cai et al., 2021), and that the Nyingoh River is also characterized by Miocene enhanced incision (Zeitler et al., 2014). Furthermore, Miocene rapid exhumation near the Lhasa River valley is also documented by inverse modeling results obtained in this study. Therefore, enhanced river incision indeed created deep river gorges that generally represent high-relief topography. The occurrence of the Yarlung River and its tributaries makes the SE Lhasa terrane a typical external drainage domain which exhibits distinct higher relief compared with large internal drainage areas in the north (Figs. 2 and 6d; Taylor et al., 2021).

In summary, in terms of topographic relief, the external (eastern Lhasa terrane) and internal drainage areas represent different (topographic) parts in the southern Tibetan Plateau. During the protracted geological evolution since the latest Cretaceous, the internal drainage area in the southern Tibetan Plateau (especially the northern Lhasa terrane) has been uplifted to the same elevation as the southern Lhasa terrane at ~30 Ma. However, different relief forms also developed within the Lhasa terrane since that time due to the differential geological processes that occurred in each subterranes. A key issue resulting in this difference is that the external drainage area experienced more recent and widespread regional basement cooling and exhumation during the late Oligocene to late Miocene (~25–5 Ma). These events, however, did not occur in the internal drainage area. These cooling events were probably related to intense tectonic uplift, fault activity and enhanced river incision that occurred in the southern Lhasa terrane.

## 6. Conclusions

Our new apatite fission track ages and inverse thermal history modeling from the eastern Lhasa terrane generally show three main accelerated basement cooling and thus exhumation events in the external drainage area (southern Tibetan Plateau) during the Cenozoic. The cooling phase occurring during the Paleocene-early Eocene (~60–48 Ma) resulted from crustal shortening and associated rock exhumation induced by accelerated northward subduction of the NeoTethys oceanic lithosphere. A subsequent cooling phase took place during the late Eocene to early Oligocene (~40–28 Ma), and it is related to the thickening and resulting erosion of the Lhasa lithosphere in response to the continuous northward indentation of the India plate into Eurasia. The latest rapid basement cooling occurred in the middle Miocene-early Pliocene (~16–4 Ma) and a combination of the activity of Luobadui-Milashan fault and enhanced incision of the Lhasa River may have invoked this event. In addition, the external and internal drainage areas in southern Tibet have contrasting reliefs. The low-temperature thermochronological data reveal that the external drainage area experienced more recent basement cooling events compared with the internal drainage area, and their diverse evolution probably initiated at ca. 30 Ma. The driving mechanisms that led to different reliefs include three aspects: (1) the intense tectonic uplift occurring in the southern Lhasa terrane, largely due to the delamination of the lithospheric mantle beneath the southern Lhasa terrane; (2) fault activity, including the movements of north-striking normal faults and several thrusts (i.e., Gangdese thrust, Great Counter thrust and local thrusts); and (3) the enhanced river incision along the Yarlung River drainage network.

## CRediT authorship contribution statement

**Wenbo Su:** Conceptualization, Investigation, Methodology, Data curation, Visualization, Writing – original draft. **Zhiyuan He:** Conceptualization, Methodology, Formal analysis, Writing – review & editing, Funding acquisition. **Linglin Zhong:** Investigation, Writing – review & editing, Funding acquisition. **Stijn Glorie:** Methodology, Writing – review & editing. **Kanghui Zhong:** Investigation, Validation. **Johan De Grave:** Supervision, Writing – review & editing, Funding acquisition.

## Declaration of Competing Interest

The authors declare that they have no known competing financial interests or personal relationships that could have appeared to influence the work reported in this paper.

## Acknowledgements

The authors would like to thank anonymous reviewers for helpful comments that improved the manuscript, and Associate Editor Nick Roberts and Editorial Advisor M. Santosh for their editorial handling. We are grateful to Hongjie Zhang and Yilong Liu for their help and cooperation during the fieldwork in 2021. Dr. Simon Nachtergaele, Ann-Eline Debeer and Jan Jurceka are thanked for assistance in sample preparation in our laboratory at Ghent University. We greatly appreciate the help provided by Dr. Bart Van Houdt and Dr. Guido Vittiglio with irradiation and neutron dosimetry at the Belgian Nuclear Research Centre in Mol (SCK-CEN, BR1 facility). We also thank Dongxu Cai and Ana Fonseca for useful discussion on this manuscript. This work is supported by National Key Research and Development Program of China (2022YFC2905001; 2018YFC0604105), the Opening Foundation of Ministry of Natural Resources Key Laboratory for Mineral Deposits Research, Chengdu University of Technology (grant number: gzck202104), and the Fund for Scientific Research - Flanders (FWO, Bilateral Project VS06520N). China Scholarship Council (201908320260; 201806190214) provided financial support for W. Su and Z. He for their research stay in Belgium. S. Glorie is supported by an Australian Research Council Future Fellowship (FT210100906). This is a contribution to the "Qomolangma Science Project" of Chengdu University of Technology.

## Appendix A. Supplementary data

Supplementary data to this article can be found online at https://doi.org/10.1016/j.gsf.2023.101610.

## References

Aitchison, J.C., Davis, A.M., Badengzhu, L., H.,, 2003. The Gangdese thrust: a phantom structure that did not raise Tibet. Terra Nova 15, 155–162. https://doi.org/10.1046/j.1365-3121.2003.00480.x.

Bian, S., Gong, J.F., Zuza, A.V., Yang, R., Chen, L., Ji, J.Q., Yu, X.J., Tian, Y.H., Yu, Z.Q., Cheng, X.G., Lin, X.B., Chen, H.L., 2022. Along-strike variation in the initiation timing of the north-trending rifts in southern Tibet as revealed from the Yadong-Gulu rift. Tectonics 41, e2021TC007091. doi: 10.1029/2021tc007091.

Bian, S., Gong, J.F., Zuza, A.V., Yang, R., Tian, Y.T., Ji, J.Q., Chen, H.L., Xu, Q.Q., Chen, L., Lin, X.B., Cheng, X.G., Tu, J.Y., Yu, X.J., 2020. Late Pliocene onset of the Cona rift, eastern Himalaya, confirms eastward propagation of extension in Himalayan-Tibetan orogen. Earth Planet. Sci. Lett. 544,. https://doi.org/10.1016/j.epsl.2020.116383 116383.

Bookhagen, B., Thiede, R.C., Strecker, M.R., 2005. Abnormal monsoon years and their control on erosion and sediment flux in the high, arid northwest Himalaya. Earth Planet. Sci. Lett. 231, 131–146. https://doi.org/10.1016/j.epsl.2004.11.014.

Cai, D.X., Wang, X.Y., Li, G.W., Zhu, W.B., Lu, H.Y., 2021. Late Cenozoic denudation and topographic evolution history of the Lhasa River drainage in Southern Tibetan Plateau: Insights from inverse thermal history modeling. Front. Earth Sci. 9,. https://doi.org/10.3389/feart.2021.636459 636459.

Cande, S.C., Patriat, P., 2015. The anticorrelated velocities of Africa and India in the Late Cretaceous and early Cenozoic. Geophys. J. Int. 200, 227–243. https://doi.org/10.1093/gji/ggu392.

Cao, K., Tian, Y.T., van der Beek, P., Wang, G.C., Shen, T.Y., Reiners, P., Bernet, M., Husson, L., 2022. Southwestward growth of plateau surfaces in eastern Tibet. Earth-Sci. Rev. 232,. https://doi.org/10.1016/j.earscirev.2022.104160 104160.

Cao, W.R., Yang, J.M., Zuza, A.V., Ji, W.Q., Ma, X.X., Chu, X., Burgess, Q.P., 2020. Crustal tilting and differential exhumation of Gangdese Batholith in southern Tibet revealed by bedrock pressures. Earth Planet. Sci. Lett. 543,. https://doi.org/10.1016/j.epsl.2020.116347 116347.

Chen, Y., Li, W., Yuan, X.H., Badal, J., Teng, J.W., 2015. Tearing of the Indian lithospheric slab beneath southern Tibet revealed by SKS-wave splitting measurements. Earth Planet. Sci. Lett. 413, 13–24. https://doi.org/10.1016/j.epsl.2014.12.041.

Chung, S.L., Liu, D.Y., Ji, J.Q., Chu, M.F., Lee, H.Y., Wen, D.J., Lo, C.H., Lee, T.Y., Qian, Q., Zhang, Q., 2003. Adakites from continental collision zones: melting of thickened lower crust beneath southern Tibet. Geology 31, 1021–1024. https://doi.org/10.1130/G19796.1.

Chung, S.L., Chu, M.F., Zhang, Y.Q., Xie, Y.W., Lo, C.H., Lee, T.Y., Lan, C.Y., Li, X.H., Zhang, Q., Wang, Y.Z., 2005. Tibetan tectonic evolution inferred from spatial and temporal variations in post-collisional magmatism. Earth-Sci. Rev. 68, 173–196. https://doi.org/10.1016/j.earscirev.2004.05.001.

Chung, S.L., Chu, M.F., Ji, J.Q., O'Reilly, S.Y., Pearson, N.J., Liu, D.Y., Lee, T.Y., Lo, C.H., 2009. The nature and timing of crustal thickening in Southern Tibet: Geochemical and zircon Hf isotopic constraints from postcollisional adakites. Tectonophysics 477, 36–48. https://doi.org/10.1016/j.tecto.2009.08.008.

Clark, M.K., House, M.A., Royden, L.H., Whipple, K.X., Burchfiel, B.C., Zhang, X., Tang, W., 2005. Late Cenozoic uplift of southeastern Tibet. Geology 33, 525–528. https://doi.org/10.1130/g21265.1.

Clark, M.K., Royden, L.H., Whipple, K.X., Burchfiel, B.C., Zhang, X., Tang, W., 2006. Use of a regional, relict landscape to measure vertical deformation of the eastern Tibetan Plateau. J. Geophys. Res. 111, F3002. https://doi.org/10.1029/2005JF000294.

Clift, P.D., Hodges, K.V., Heslop, D., Hannigan, R., Van Long, H., Calves, G., 2008. Correlation of Himalayan exhumation rates and Asian monsoon intensity. Nat. Geosci. 1, 875–880. https://doi.org/10.1038/ngeo351.

Clift, P.D., Webb, A.A.G., 2018. A history of the Asian monsoon and its interactions with solid Earth tectonics in Cenozoic South Asia. Geol. Soc. Spec. Publ. 483, 631–652. https://doi.org/10.1144/sp483.1.

Cloetingh, S.A.P.L., Ziegler, P.A., Bogaard, P.J.F., Andriessen, P.A.M., Artemieva, I.M., Bada, G., van Balen, R.T., Beekman, F., Ben-Avraham, Z., Brun, J.P., Bunge, H.P., Burov, E.B., Carbonell, R., Faccenna, C., Friedrich, A., Gallart, J., Green, A.G., Heidbach, O., Jones, A.G., Matenco, L., Mosar, J., Oncken, O., Pascal, C., Peters, G., Sliaupa, S., Soesoo, A., Spakman, W., Stephenson, R.A., Thybo, H., Torsvik, T., de Vicente, G., Wenzel, F., Wortel, M.J.R., 2007. TOPO-EUROPE: The geoscience of coupled deep Earth-surface processes. Global Planet. Change 58, 1–118. https://doi.org/10.1016/j.gloplacha.2007.02.008.

Copeland, P., Harrison, T.M., Pan, Y., Kidd, W.S.F., Roden, M., Zhang, Y.Q., 1995. Thermal evolution of the Gangdese batholith, southern Tibet: A history of episodic unroofing. Tectonics 14, 223–236. https://doi.org/10.1029/94TC01676.

Dai, J.G., Wang, C.S., Hourigan, J., Li, Z.J., Zhuang, G.S., 2013. Exhumation history of the Gangdese Batholith, Southern Tibetan Plateau: evidence from apatite and zircon (U-Th)/He thermochronology. J. Geol. 121, 155–172. https://doi.org/10.1086/669250.

Dai, J.G., Fox, M., Han, X., Tremblay, M.M., Xu, S.Y., Shuster, D.L., Liu, B.R., Zhang, J.W., Wang, C.S., 2021. Two stages of accelerated exhumation in the middle reach of the Yarlung River, Southern Tibet since the mid-miocene. Tectonics 40, 1–17. https://doi.org/10.1029/2020tc006618.

Dazé, A., Lee, J.K.W., Villeneuve, M., 2003. An intercalibration study of the Fish Canyon sanidine and biotite $^{40}Ar/^{39}Ar$ standards and some comments on the age of the Fish Canyon Tuff. Chem. Geol. 199, 111–127. https://doi.org/10.1016/s0009-2541(03)00079-2.

De Corte, F., Bellemans, F., Van den Haute, P., Ingelbrecht, C., Nicholl, C., 1998. A new U doped glass certified by the European Commission for the calibration of fission-track dating. In: Advances in Fission-track Geochronology. Springer, pp. 67–78.

De Grave, J., Glorie, S., Vermaercke, P., Vittiglio, G., 2010. A 'new' irradiation facility for FT applications at the Belgian Nuclear Research Centre: the BR1 reactor. In: 12th International conference on Thermochronology (Thermo 2010).

DeCelles, P.G., Quade, J., Kapp, P., Fan, M., Dettman, D.L., Ding, L., 2007. High and dry in central Tibet during the Late Oligocene. Earth Planet. Sci. Lett. 253, 389–401. https://doi.org/10.1016/j.epsl.2006.11.001.

DeCelles, P.G., Kapp, P., Quade, J., Gehrels, G.E., 2011. Oligocene-Miocene Kailas basin, southwestern Tibet: Record of postcollisional upper-plate extension in the Indus-Yarlung suture zone. Geol. Soc. Am. Bull. 123, 1337–1362. https://doi.org/10.1130/b30258.1.

DeCelles, P.G., Kapp, P., Gehrels, G.E., Ding, L., 2014. Paleocene-Eocene foreland basin evolution in the Himalaya of southern Tibet and Nepal: Implications for the age of initial India-Asia collision. Tectonics 33, 824–849. https://doi.org/10.1002/2014tc003522.

DePaolo, D.J., Harrison, T.M., Wielicki, M., Zhao, Z.D., Zhu, D.C., Zhang, H.F., Mo, X.X., 2019. Geochemical evidence for thin syn-collision crust and major crustal thickening between 45 and 32 Ma at the southern margin of Tibet. Gondwana Res. 73, 123–135. https://doi.org/10.1016/j.gr.2019.03.011.

Ding, L., Kapp, P., Cai, F.L., Garzione, C.N., Xiong, Z.Y., Wang, H.Q., Wang, C., 2022. Timing and mechanisms of Tibetan Plateau uplift. Nat. Rev. Earth Environ. doi: 10.1038/s43017-022-00318-4.

Ding, L., Kapp, P., Wan, X.Q., 2005. Paleocene-Eocene record of ophiolite obduction and initial India-Asia collision, south central Tibet. Tectonics 24, TC3001. https://doi.org/10.1029/2004tc001729.

Ding, L., Xu, Q., Yue, Y.H., Wang, H.Q., Cai, F.L., Li, S., 2014. The Andean-type Gangdese Mountains: Paleoelevation record from the Paleocene-Eocene Linzhou Basin. Earth Planet. Sci. Lett. 392, 250–264. https://doi.org/10.1016/j.epsl.2014.01.045.

Donelick, R.A., Miller, D.S., 1991. Enhanced TINT fission track densities in low spontaneous track density apatites using 252Cf-derived fission fragment tracks: A model and experimental observations. Nucl. Tracks Radiat. Meas. 18, 301–307. https://doi.org/10.1016/1359-0189(91)90022-A.

Donelick, R.A., O'Sullivan, P.B., Ketcham, R.A., 2005. Apatite fission-track analysis. Rev. Mineral. Geochem. 58, 49–94. https://doi.org/10.2138/rmg.2005.58.3.

Dong, X., Zhang, Z.M., Santosh, M., 2010. Zircon U-Pb Chronology of the Nyingtri Group, Southern Lhasa Terrane, Tibetan Plateau: Implications for Grenvillian and Pan-African provenance and mesozoic-cenozoic metamorphism. J. Geol. 118, 677–690. https://doi.org/10.1086/656355.

Fang, X.M., Dupont Nivet, G., Wang, C.S., Song, C.H., Meng, Q.Q., Zhang, W.L., Nie, J.S., Zhang, T., Mao, Z.Q., Chen, Y., 2020. Revised chronology of central Tibet uplift (Lunpola Basin). Sci. Adv. 6,. https://doi.org/10.1126/sciadv.aba7298 eaba7298.

Fielding, E., Isacks, B., Barazangi, M., Duncan, C., 1994. How flat is Tibet? Geology 22, 163–167. https://doi.org/10.1130/0091-7613(1994)022<0163:HFIT>2.3.CO;2.

Galbraith, R.F., 1981. On statistical models for fission track counts. Math. Geol. 13, 471–478. https://doi.org/10.1007/BF01034498.

Gallagher, K., 2012. Transdimensional inverse thermal history modeling for quantitative thermochronology. J. Geophys. Res. 117, B02408. https://doi.org/10.1029/2011jb008825.

Gallagher, K., Charvin, K., Nielsen, S., Sambridge, M., Stephenson, J., 2009. Markov chain Monte Carlo (MCMC) sampling methods to determine optimal models, model resolution and model choice for Earth Science problems. Mar. Pet. Geol. 26, 525–535. https://doi.org/10.1016/j.marpetgeo.2009.01.003.

Ge, Y.K., Dai, J.G., Wang, C.S., Li, Y.L., Xu, G.Q., Danisik, M., 2017. Cenozoic thermotectonic evolution of the Gangdese batholith constrained by low-temperature thermochronology. Gondwana Res. 41, 451–462. https://doi.org/10.1016/j.gr.2016.05.006.

Gibbons, A.D., Zahirovic, S., Müller, R.D., Whittaker, J.M., Yatheesh, V., 2015. A tectonic model reconciling evidence for the collisions between India, Eurasia and intra-oceanic arcs of the central-eastern Tethys. Gondwana Res. 28, 451–492. https://doi.org/10.1016/j.gr.2015.01.001.

Gleadow, A., Duddy, I., Green, P.F., Lovering, J., 1986. Confined fission track lengths in apatite: a diagnostic tool for thermal history analysis. Contrib. Mineral. Petrol. 94, 405–415. https://doi.org/10.1007/BF00376334.

Gleadow, A.J.W., Lovering, J.F., 1977. Geometry factor for external detectors in fission track dating. Nuclear Track Detection 1, 99–106. https://doi.org/10.1016/0145-224X(77)90003-5.

Green, P.F., Duddy, I.R., Gleadow, A.J., Lovering, J.F., 1989. Apatite fission-track analysis as a paleotemperature indicator for hydrocarbon exploration. In: Thermal History of Sedimentary Basins. Springer, pp. 181–195.

Guo, X.Y., Gao, R., Zhao, J.M., Xu, X., Lu, Z.W., Klemperer, S.L., Liu, H.B., 2018. Deep-seated lithospheric geometry in revealing collapse of the Tibetan Plateau. Earth-Sci. Rev. 185, 751–762. https://doi.org/10.1016/j.earscirev.2018.07.013.

Haider, V.L., Dunkl, I., Eynatten, H.v., Ding, L., Frei, D., Zhang, L.Y., 2013. Cretaceous to Cenozoic evolution of the northern Lhasa Terrane and the Early Paleogene development of peneplains at Nam Co, Tibetan Plateau. J. Asian Earth Sci. 70-71, 79-98. doi: 10.1016/j.jseaes.2013.03.005.

Han, Z.P., Sinclair, H.D., Li, Y.L., Wang, C.S., Tao, Z., Qian, X.Y., Ning, Z.J., Zhang, J.W., Wen, Y.X., Lin, J., Zhang, B.S., Xu, M., Dai, J.G., Zhou, A., Liang, H.M., Cao, S., 2019. Internal drainage has sustained low-relief Tibetan landscapes since the Early Miocene. Geophys. Res. Lett. 46, 8741–8752. https://doi.org/10.1029/2019gl083019.

Harrison, T.M., Copeland, P., Kidd, W.S.F., Lovera, O.M., 1995. Activation of the Nyainqentanghla shear zone: Implications for uplift of the southern Tibetan Plateau. Tectonics 14, 658–676. https://doi.org/10.1029/95TC00608.

Harrison, T.M., Yin, A., Grove, M., Lovera, O.M., Ryerson, F.J., Zhou, X.H., 2000. The Zedong Window: A record of superposed Tertiary convergence in southeastern Tibet. J. Geophys. Res. 105, 19211–19230. https://doi.org/10.1029/2000jb900078.

He, S.D., Kapp, P., DeCelles, P.G., Gehrels, G.E., Heizler, M., 2007. Cretaceous-Tertiary geology of the Gangdese Arc in the Linzhou area, southern Tibet. Tectonophysics 433, 15–37. https://doi.org/10.1016/j.tecto.2007.01.005.

He, Z.Y., Wang, B., Su, W.B., Glorie, S., Ni, X.H., Liu, J.S., Cai, D.X., Zhong, L.L., De Grave, J., 2022. Meso-Cenozoic thermo-tectonic evolution of the Yili block within the Central Asian Orogenic Belt (NW China): Insights from apatite fission track thermochronology. Tectonophysics 823,. https://doi.org/10.1016/j.tecto.2021.229194 229194.

Hetzel, R., Dunkl, I., Haider, V., Strobl, M., von Eynatten, H., Ding, L., Frei, D., 2011. Peneplain formation in southern Tibet predates the India-Asia collision and plateau uplift. Geology 39, 983–986. https://doi.org/10.1130/g32069.1.

Hu, X.M., Garzanti, E., Wang, J.G., Huang, W.T., An, W., Webb, A., 2016a. The timing of India-Asia collision onset – Facts, theories, controversies. Earth-Sci. Rev. 160, 264–299. https://doi.org/10.1016/j.earscirev.2016.07.014.

Hu, X.M., Wang, J.G., BouDagher-Fadel, M., Garzanti, E., An, W., 2016b. New insights into the timing of the India – Asia collision from the Paleogene Quxia and Jialazi formations of the Xigaze forearc basin. South Tibet. Gondwana Res. 32, 76–92. https://doi.org/10.1016/j.gr.2015.02.007.

Huang, W.T., Lippert, P.C., Reiners, P.W., Quade, J., Kapp, P., Ganerød, M., Guo, Z.J., van Hinsbergen, D.J.J., 2022. Hydrothermal events in the Linzizong Group: Implications for Paleogene exhumation and paleoaltimetry of the southern Tibetan Plateau. Earth Planet. Sci. Lett. 583,. https://doi.org/10.1016/j.epsl.2022.117390 117390.

Hurford, A.J., 1990. Standardization of fission track dating calibration: Recommendation by the Fission Track Working Group of the I.U.G.S. Subcommission on Geochronology. Chem. Geol. 80, 171–178. https://doi.org/10.1016/0168-9622(90)90025-8.

Hurford, A.J., Green, P.F., 1983. The zeta age calibration of fission-track dating. Chem. Geol. 41, 285–317. https://doi.org/10.1016/S0009-2541(83)80026-6.

Ingalls, M., Rowley, D., Olack, G., Currie, B., Li, S., Schmidt, J., Tremblay, M., Polissar, P., Shuster, D.L., Lin, D., Colman, A., 2018. Paleocene to Pliocene low-latitude, high-elevation basins of southern Tibet: Implications for tectonic models of India-Asia collision, Cenozoic climate, and geochemical weathering. Geol. Soc. Am. Bull. 130, 307–330. https://doi.org/10.1130/b31723.1.

Ji, W.Q., Wu, F.Y., Chung, S.L., Li, J.X., Liu, C.Z., 2009. Zircon U-Pb geochronology and Hf isotopic constraints on petrogenesis of the Gangdese batholith, southern Tibet. Chem. Geol. 262, 229–245. https://doi.org/10.1016/j.chemgeo.2009.01.020.

Kapp, P., DeCelles, P.G., 2019. Mesozoic-Cenozoic geological evolution of the Himalayan-Tibetan orogen and working tectonic hypotheses. Am. J. Sci. 319, 159–254. https://doi.org/10.2475/03.2019.01.

Kapp, P., Murphy, M.A., Yin, A., Harrison, T.M., Ding, L., Guo, J.H., 2003. Mesozoic and Cenozoic tectonic evolution of the Shiquanhe area of western Tibet. Tectonics 22, 1029. https://doi.org/10.1029/2001tc001332.

Kapp, P., DeCelles, P.G., Leier, A.L., Fabijanic, J.M., He, S., Pullen, A., Gehrels, G.E., Ding, L., 2007. The Gangdese retroarc thrust belt revealed. GSA Today 17, 4–9. https://doi.org/10.1130/gsat01707a.1.

Kelly, S., Beaumont, C., Butler, J.P., 2020. Inherited terrane properties explain enigmatic post-collisional Himalayan-Tibetan evolution. Geology 48, 8–14. https://doi.org/10.1130/g46701.1.

Ketcham, R.A., 2005. Forward and inverse modeling of low-temperature thermochronometry data. Rev. Mineral. Geochem. 58, 275–314. https://doi.org/10.2138/rmg.2005.58.11.

Ketcham, R.A., Carter, A., Donelick, R.A., Barbarand, J., Hurford, A.J., 2007. Improved modeling of fission-track annealing in apatite. Am. Mineral. 92, 799–810. https://doi.org/10.2138/am.2007.2281.

Laske, G., Masters, G., Ma, Z.T., Pasyanos, M., 2013. Update on CRUST1.0 - A 1-degree Global Model of Earth's Crust. In: EGU General Assembly. p 2658.

Laskowski, A.K., Kapp, P., Ding, L., Campbell, C., Liu, X.H., 2017. Tectonic evolution of the Yarlung suture zone, Lopu Range region, southern Tibet. Tectonics 36, 108–136. https://doi.org/10.1002/2016tc004334.

Laskowski, A.K., Kapp, P., Cai, F.L., 2018. Gangdese culmination model: Oligocene-Miocene duplexing along the India-Asia suture zone, Lazi region, southern Tibet. Geol. Soc. Am. Bull. 130, 1355–1376. https://doi.org/10.1130/B31834.1.

Leary, R.J., Orme, D.A., Laskowski, A.K., DeCelles, P.G., Kapp, P., Carrapa, B., Dettinger, M., 2016. Along-strike diachroneity in deposition of the Kailas Formation in central southern Tibet: Implications for Indian slab dynamics. Geosphere 12, 1198–1223. https://doi.org/10.1130/ges01325.1.

Lee, H.Y., Chung, S.L., Lo, C.H., Ji, J.Q., Lee, T.Y., Qian, Q., Zhang, Q., 2009. Eocene Neotethyan slab breakoff in southern Tibet inferred from the Linzizong volcanic record. Tectonophysics 477, 20–35. https://doi.org/10.1016/j.tecto.2009.02.031.

Li, H.A., Dai, J.G., Xu, S.Y., Liu, B.R., Han, X., Wang, Y.N., Wang, C.S., 2019. The formation and expansion of the eastern Proto-Tibetan Plateau: Insights from low-temperature thermochronology. J. Asian Earth Sci. 183,. https://doi.org/10.1016/j.jseaes.2019.103975 103975.

Li, G.W., Kohn, B., Sandiford, M., Xu, Z.Q., Wei, L.J., 2015a. Constraining the age of Liuqu Conglomerate, southern Tibet: implications for evolution of the India-Asia collision zone. Earth Planet. Sci. Lett. 426, 259–266. https://doi.org/10.1016/j.epsl.2015.06.010.

Li, G.W., Kohn, B., Sandiford, M., Xu, Z.Q., Tian, Y.T., Seiler, C., 2016. Synorogenic morphotectonic evolution of the Gangdese batholith, South Tibet: Insights from low-temperature thermochronology. Geochem. Geophys. Geosyst. 17, 101–112. https://doi.org/10.1002/2015gc006047.

Li, J.G., Pan, F.C., 2011. Tibet Autonomous Region 1: 250 ,000 construction structure map of Zedang County. Geological Survey Institute of Tibet Autonomous Region.

Li, J.T., Song, X.D., 2018. Tearing of Indian mantle lithosphere from high-resolution seismic images and its implications for lithosphere coupling in southern Tibet. PNAS 115, 8296–8300. https://doi.org/10.1073/pnas.1717258115.

Li, G.W., Tian, Y.T., Kohn, B.P., Sandiford, M., Xu, Z.Q., Cai, Z.H., 2015b. Cenozoic low temperature cooling history of the Northern Tethyan Himalaya in Zedang, SE Tibet and its implications. Tectonophysics 643, 80–93. https://doi.org/10.1016/j.tecto.2014.12.014.

Li, C., Zhao, Z.B., Lu, H.J., Li, H.B., 2022. Late Mesozoic-Cenozoic multistage exhumation of the central Bangong-Nujiang Suture. Central Tibet. Tectonophys. 827,. https://doi.org/10.1016/j.tecto.2022.229268 229268.

Liang, X.F., Chen, Y., Tian, X.B., Chen, Y.J., Ni, J., Gallegos, A., Klemperer, S.L., Wang, M. L., Xu, T., Sun, C.Q., Si, S.K., Lan, H.Q., Teng, J.W., 2016. 3D imaging of subducting and fragmenting Indian continental lithosphere beneath southern and central Tibet using body-wave finite-frequency tomography. Earth Planet. Sci. Lett. 443, 162–175. https://doi.org/10.1016/j.epsl.2016.03.029.

Liu-Zeng, J., Tapponnier, P., Gaudemer, Y., Ding, L., 2008. Quantifying landscape differences across the Tibetan plateau: Implications for topographic relief evolution. J. Geophys. Res. 113, F04018. https://doi.org/10.1029/2007JF000897.

Liu-Zeng, J., Zhang, J.Y., Ge, Y.K., Wang, W., Zeng, L.S., Gen, L., Lin, X., 2018a. Tectonic geomorphology: An interdisciplinary study of the interaction among tectonic climatic and surface processes. Chin. Sci. Bull. 63, 3070–3088. https://doi.org/10.1360/n972018-00498.

Liu-Zeng, J., Zhang, J.Y., McPhillips, D., Reiners, P., Wang, W., Pik, R., Zeng, L.S., Hoke, G., Xie, K.J., Xiao, P., Zheng, D.W., Ge, Y.K., 2018b. Multiple episodes of fast exhumation since Cretaceous in southeast Tibet, revealed by low-temperature thermochronology. Earth Planet. Sci. Lett. 490, 62–76. https://doi.org/10.1016/j.epsl.2018.03.011.

Lu, Z.W., Guo, X.Y., Gao, R., Murphy, M.A., Huang, X.F., Xu, X., Li, S.Z., Li, W.H., Zhao, J. M., Li, C.S., Xiang, B., 2022. Active construction of southernmost Tibet revealed by deep seismic imaging. Nat. Commun. 13, 3143. https://doi.org/10.1038/s41467-022-30887-3.

Maussion, F., Finkelnburg, R., Curio, J., Collier, E., Mölg, T., Scherer, D., 2014. Precipitation seasonality and variability over the tibetan plateau as resolved by the high Asia reanalysis. J. Clim. 27, 1910–1927. https://doi.org/10.1175/jcli-d-13-00282.1.

McDowell, F.W., McIntosh, W.C., Farley, K.A., 2005. A precise $^{40}Ar–^{39}Ar$ reference age for the Durango apatite (U–Th)/He and fission-track dating standard. Chem. Geol. 214, 249–263. https://doi.org/10.1016/j.chemgeo.2004.10.002.

Meng, F.Y., Zhao, Z.D., Zhu, D.C., Mo, X.X., Guan, Q., Huang, Y., Dong, G.C., Zhou, S., DePaolo, D.J., Harrison, T.M., Zhang, Z.C., Liu, J.L., Liu, Y.S., Hu, Z.C., Yuan, H.L., 2014. Late Cretaceous magmatism in Mamba area, central Lhasa subterrane: Products of back-arc extension of Neo-Tethyan Ocean? Gondwana Res. 26, 505–520. https://doi.org/10.1016/j.gr.2013.07.017.

Mo, X.X., Niu, Y.L., Dong, G.C., Zhao, Z.D., Hou, Z.Q., Zhou, S., Ke, S., 2008. Contribution of syncollisional felsic magmatism to continental crust growth: A case study of the Paleogene Linzizong volcanic Succession in southern Tibet. Chem. Geol. 250, 49–67. https://doi.org/10.1016/j.chemgeo.2008.02.003.

Murphy, M.A., Yin, A., 2003. Structural evolution and sequence of thrusting in the Tethyan fold-thrust belt and Indus-Yalu suture zone, southwest Tibet. Geol. Soc. Am. Bull. 115, 21–34. https://doi.org/10.1130/0016-7606(2003)115<0021:SEASOT>2.0.CO;2.

Nachtergaele, S., De Pelsmaeker, E., Glorie, S., Zhimulev, F., Jolivet, M., Danišík, M., Buslov, M.M., De Grave, J., 2018. Meso-Cenozoic tectonic evolution of the Talas-Fergana region of the Kyrgyz Tien Shan revealed by low-temperature basement and detrital thermochronology. Geosci. Front. 9, 1495–1514. https://doi.org/10.1016/j.gsf.2017.11.007.

Nie, J.S., Ruetenik, G., Gallagher, K., Hoke, G., Garzione, C.N., Wang, W.T., Stockli, D., Hu, X.F., Wang, Z., Wang, Y., Stevens, T., Danišík, M., Liu, S.P., 2018. Rapid incision of the Mekong River in the middle Miocene linked to monsoonal precipitation. Nat. Geosci. 11, 944–948. https://doi.org/10.1038/s41561-018-0244-z.

Nimaciren, Xie, Y.W., Sha, Z.L., Xiluolangjie, Qiangbazaxi, Peng, D.P., Gesangsuolang, Luosongzhandui, 2005. 1: 250, 000 geological report of Nagqu County with geological map. Xizang Institute of Geological Survey, Lhasa (in Chinese).

Pan, Y., Copeland, P., Roden, M.K., Kidd, W.S.F., Harrison, T.M., 1993. Thermal and unroofing history of the Lhasa area, southern Tibet—evidence from apatite fission track thermochronology. Nucl. Tracks Radiat. Meas. 21, 543–554. https://doi.org/10.1016/1359-0189(93)90195-F.

Pan, G.T., Ding, J., Yao, D.S., Wang, L.Q., 2004. Guidebook of 1:1,500,000 geologic map of the Qinghai-Xizang (Tibet) plateau and adjacent areas. Cartographic Publishing House, Chengdu, China (in Chinese).

Reiners, P.W., Ehlers, T.A., 2005. Low-Temperature Thermochronology: Techniques, Interpretations, and Applications. Walter de Gruyter GmbH & Co KG, pp. 1–622.

Rohrmann, A., Kapp, P., Carrapa, B., Reiners, P.W., Guynn, J., Ding, L., Heizler, M., 2012. Thermochronologic evidence for plateau formation in central Tibet by 45 Ma. Geology 40, 187–190. https://doi.org/10.1130/g32530.1.

Rowley, D.B., Currie, B.S., 2006. Palaeo-altimetry of the late Eocene to Miocene Lunpola basin, central Tibet. Nature 439, 677–681. https://doi.org/10.1038/nature04506.

Sanyal, P., Sarkar, A., Bhattacharya, S.K., Kumar, R., Ghosh, S.K., Agrawal, S., 2010. Intensification of monsoon, microclimate and asynchronous C4 appearance: Isotopic evidence from the Indian Siwalik sediments. Palaeogeog. Palaeoclimatol. Palaeoecol. 296, 165–173. https://doi.org/10.1016/j.palaeo.2010.07.003.

Strobl, M., Hetzel, R., Niedermann, S., Ding, L., Zhang, L., 2012. Landscape evolution of a bedrock peneplain on the southern Tibetan Plateau revealed by in situ-produced cosmogenic $^{10}Be$ and $^{21}Ne$. Geomorphology 153–154, 192–204. https://doi.org/10.1016/j.geomorph.2012.02.024.

Styron, R.H., Taylor, M.H., Sundell, K.E., Stockli, D.F., Oalmann, J.A.G., Möller, A., McCallister, A.T., Liu, D.L., Ding, L., 2013. Miocene initiation and acceleration of extension in the South Lunggar rift, western Tibet: Evolution of an active detachment system from structural mapping and (U-Th)/He thermochronology. Tectonics 32, 880–907. https://doi.org/10.1002/tect.20053.

Su, W.B., He, Z.Y., Zhong, L.L., Glorie, S., Zhong, K.H., Jepson, G., De Grave, J., 2022. Late Oligocene - Miocene morpho-tectonic evolution of the central Gangdese batholith constrained by low-temperature thermochronology. Tectonophysics 840,. https://doi.org/10.1016/j.tecto.2022.229559 229559.

Su, T., Spicer, R.A., Wu, F.X., Farnsworth, A., Huang, J., Del Rio, C., Deng, T., Ding, L., Deng, W.Y., Huang, Y.J., Hughes, A., Jia, L.B., Jin, J.H., Li, S.F., Liang, S.Q., Liu, J., Liu, X.Y., Sherlock, S., Spicer, T., Srivastava, G., Tang, H., Valdes, P., Wang, T.X., Widdowson, M., Wu, M.X., Xing, Y.W., Xu, C.L., Yang, J., Zhang, C., Zhang, S.T., Zhang, X.W., Zhao, F., Zhou, Z.K., 2020. A Middle Eocene lowland humid subtropical "Shangri-La" ecosystem in central Tibet. Proc. Nat. Acad. Sci. U.S.A. 117, 32989–32995. https://doi.org/10.1073/pnas.2012647117.

Sun, X.J., Wang, P.X., 2005. How old is the Asian monsoon system?—Palaeobotanical records from China. Palaeogeog. Palaeoclimatol. Palaeoecol. 222, 181–222. https://doi.org/10.1016/j.palaeo.2005.03.005.

Sundell, K.E., Taylor, M.H., Styron, R.H., Stockli, D.F., Kapp, P., Hager, C., Liu, D.L., Ding, L., 2013. Evidence for constriction and Pliocene acceleration of east-west

extension in the North Lunggar rift region of west central Tibet. Tectonics 32, 1454–1479. https://doi.org/10.1002/tect.20086.
Tang, M., Ji, W.Q., Chu, X., Wu, A.B., Chen, C., 2020. Reconstructing crustal thickness evolution from europium anomalies in detrital zircons. Geology 49, 76–80. https://doi.org/10.1130/g47745.1.
Tapponnier, P., Xu, Z.Q., Roger, F., Meyer, B., Arnaud, N., Wittlinger, G., Yang, J.S., 2001. Oblique stepwise rise and growth of the Tibet Plateau. Science 294, 1671–1677. https://doi.org/10.1126/science.105978.
Taylor, M., Forte, A., Laskowski, A., Ding, L., 2021. Active Uplift of Southern Tibet Revealed. GSA Today 31, 4–10. https://doi.org/10.1130/gsatg487a.1.
Tremblay, M.M., Fox, M., Schmidt, J.L., Tripathy-Lang, A., Wielicki, M.M., Harrison, T. M., Zeitler, P.K., Shuster, D.L., 2015. Erosion in southern Tibet shut down at approximately 10 Ma due to enhanced rock uplift within the Himalaya. Proc. Nat. Acad. Sci. U.S.A. 112, 12030–12035. https://doi.org/10.1073/pnas.1515652112.
van Hinsbergen, D.J.J., Steinberger, B., Doubrovine, P.V., Gassmöller, R., 2011. Acceleration and deceleration of India-Asia convergence since the Cretaceous: Roles of mantle plumes and continental collision. J. Geophys. Res. 116, B06101. https://doi.org/10.1029/2010jb008051.
Van Ranst, G., Baert, P., Fernandes, A.C., De Grave, J., 2020a. Technical note: Nikon–TRACK Flow, a new versatile microscope system for fission track analysis. Geochronology 2, 93–99. https://doi.org/10.5194/gchron-2-93-2020.
Van Ranst, G., Pedrosa-Soares, A.C., Novo, T., Vermeesch, P., De Grave, J., 2020b. New insights from low-temperature thermochronology into the tectonic and geomorphologic evolution of the south-eastern Brazilian highlands and passive margin. Geosci. Front. 11, 303–324. https://doi.org/10.1016/j.gsf.2019.05.011.
Wagner, G., Van den haute, P., 1992. Fission-track dating. In. Springer Science & Business Media, pp 1-293.
Vermeesch, P., 2009. RadialPlotter: A Java application for fission track, luminescence and other radial plots. Radiat. Meas. 44, 409–410.
Wang, C., Ding, L., Zhang, L.Y., Kapp, P., Pullen, A., Yue, Y.H., 2016. Petrogenesis of Middle-Late Triassic volcanic rocks from the Gangdese belt, southern Lhasa terrane: Implications for early subduction of Neo-Tethyan oceanic lithosphere. Lithos 262, 320–333. https://doi.org/10.1016/j.lithos.2016.07.021.
Wang, C.S., Li, X.H., Liu, Z.F., Li, Y.L., Jansa, L., Dai, J.G., Wei, Y.S., 2012. Revision of the Cretaceous-Paleogene stratigraphic framework, facies architecture and provenance of the Xigaze forearc basin along the Yarlung Zangbo suture zone. Gondwana Res. 22, 415–433. https://doi.org/10.1016/j.gr.2011.09.014.
Wang, R., Tafti, R., Hou, Z.Q., Shen, Z.C., Guo, N., Evans, N.J., Jeon, H., Li, Q.Y., Li, W.L., 2017b. Across-arc geochemical variation in the Jurassic magmatic zone, Southern Tibet: Implication for continental arc-related porphyry Cu Au mineralization. Chem. Geol. 451, 116–134. https://doi.org/10.1016/j.chemgeo.2017.01.010.
Wang, G., Wei, W.B., Ye, G.F., Jin, S., Jing, J.E., Zhang, L.T., Dong, H., Xie, C.L., Omisore, B.O., Guo, Z.Q., 2017a. 3-D electrical structure across the Yadong-Gulu rift revealed by magnetotelluric data: New insights on the extension of the upper crust and the geometry of the underthrusting Indian lithospheric slab in southern Tibet. Earth Planet. Sci. Lett. 474, 172–179. https://doi.org/10.1016/j.epsl.2017.06.027.
Wang, Y., Zhang, X.M., Sun, L.X., Wan, J.L., 2007. Cooling history and tectonic exhumation stages of the south-central Tibetan Plateau (China): Constrained by 40Ar/39Ar and apatite fission track thermochronology. J. Asian Earth Sci. 29, 266–282. https://doi.org/10.1016/j.jseaes.2005.11.001.
Whipple, K.X., 2009. The influence of climate on the tectonic evolution of mountain belts. Nat. Geosci. 2, 97–104. https://doi.org/10.1038/ngeo413.
Willett, S.D., Hovius, N., Brandon, M.T., Fisher, D.M., 2006. Tectonics, Climate, and Landscape Evolution. In: Willett, S.D. (Ed.), Tectonics, Climate, and Landscape Evolution. The Geological Society of America, USA, pp. 1–429.
Wolff, R., Hetzel, R., Dunkl, I., Xu, Q., Bröcker, M., Anczkiewicz, A.A., 2019. High-Angle Normal Faulting at the Tangra Yumco Graben (Southern Tibet) since ~15 Ma. J. Geol. 127, 15–36. https://doi.org/10.1086/700406.
Xiong, Z.Y., Liu, X.H., Ding, L., Farnsworth, A., Spicer, R.A., Xu, Q., Valdes, P., He, S.L., Zeng, D., Wang, C., Li, Z.Y., Guo, X.D., Su, T., Zhao, C.Y., Wang, H.Q., Yue, Y.H., 2022. The rise and demise of the Paleogene Central Tibetan Valley. Sci. Adv. 8, eabj0944. https://doi.org/10.1126/sciadv.abj0944.
Xu, Q., Ding, L., Hetzel, R., Yue, Y., Rades, E.F., 2015. Low elevation of the northern Lhasa terrane in the Eocene: Implications for relief development in south Tibet. Terra Nova 27, 458–466. https://doi.org/10.1111/ter.12180.
Xue, W.W., Najman, Y., Hu, X.M., Persano, C., Stuart, F.M., Li, W., Ma, A.L., Wang, Y., 2022. Late Cretaceous to Late Eocene Exhumation in the Nima Area, Central Tibet: Implications for Development of Low Relief Topography of the Tibetan Plateau. Tectonics 41, e2021TC006989. doi: 10.1029/2021tc006989.
Yang, D.M., 2004. Geological map of the 1:250,000 regional geological survey in Menba area (H46C002002). Jilin University, Jilin.
Yin, A., Harrison, T.M., Ryerson, F.J., Wenji, C., Kidd, W.S.F., Copeland, P., 1994. Tertiary structural evolution of the Gangdese Thrust System, southeastern Tibet. J. Geophys. Res. 99, 18175–18201. https://doi.org/10.1029/94jb00504.
Yin, A., Harrison, T.M., Murphy, M.A., Grove, M., Nie, S., Ryerson, F.J., Wang, X.F., Chen, Z.L., 1999. Tertiary deformation history of southeastern and southwestern Tibet during the Indo-Asian collision. Geol. Soc. Am. Bull. 111, 1644–1664. https://doi.org/10.1130/0016-7606(1999)111<1644:TDHOSA>2.3.CO;2.
Yin, A., Harrison, T.M., 2000. Geologic Evolution of The Himalayan-Tibetan Orogen. Annu. Rev. Earth Planet. Sci. 28, 211–280. https://doi.org/10.1146/annurev.earth.28.1.211.
Yuan, X.P., Huppert, K.L., Braun, J., Shen, X., Liu-Zeng, J., Guerit, L., Wolf, S.G., Zhang, J.F., Jolivet, M., 2021. Propagating uplift controls on high-elevation, lowrelief landscape formation in the southeast Tibetan Plateau. Geology 50, 60–65. https://doi.org/10.1130/G49022.1.
Zeitler, P.K., Meltzer, A.S., Brown, L., Kidd, W.S., Lim, C., Enkelmann, E., 2014. Tectonics and topographic evolution of Namche Barwa and the easternmost Lhasa block, Tibet. In: Toward an improved understanding of uplift mechanisms and the elevation history of the Tibetan Plateau. Geological Society of America Special Papers, pp 23-58.
Zhang, Z.M., Dong, X., Liu, F., Lin, Y.H., Yan, R., He, Z.Y., Santosh, M., 2012. The making of Gondwana: Discovery of 650Ma HP granulites from the North Lhasa, Tibet. Precambrian Res. 212–213, 107–116. https://doi.org/10.1016/j.precamres.2012.04.018.
Zhang, J.W., Li, H.A., Zhang, H.P., Xu, X.Y., 2020. Research progress in cenozoic N-S striking rifts in Tibetan Plateau. Advances in Earth Science 35, 848-862 (in Chinese with English abstract). doi: 10.11867/j.issn.1001-8166.2020.064.
Zhao, Z.D., Mo, X.X., Dilek, Y., Niu, Y.L., DePaolo, D.J., Robinson, P., Zhu, D.C., Sun, C.G., Dong, G.C., Zhou, S., 2009. Geochemical and Sr–Nd–Pb–O isotopic compositions of the post-collisional ultrapotassic magmatism in SW Tibet: Petrogenesis and implications for India intra-continental subduction beneath southern Tibet. Lithos 113, 190–212. https://doi.org/10.1016/j.lithos.2009.02.004.
Zhao, J.X., Qin, K.Z., Li, G.M., Cao, M.J., Evans, N.J., McInnes, B.I.A., Li, J.X., Xiao, B., Chen, L., 2015. The exhumation history of collision-related mineralizing systems in Tibet: Insights from thermal studies of the Sharang and Yaguila deposits, central Lhasa. Ore Geol. Rev. 65, 1043–1061. https://doi.org/10.1016/j.oregeorev.2014.09.026.
Zhao, J.M., Yuan, X.H., Liu, H.B., Kumar, P., Pei, S.P., Kind, R., Zhang, Z.J., Teng, J.W., Ding, L., Gao, X., Xu, Q., Wang, W., 2010. The boundary between the Indian and Asian tectonic plates below Tibet. Proc. Nat. Acad. Sci. U.S.A. 107, 11229–11233. https://doi.org/10.1073/pnas.1001921107.
Zhao, T.P., Zhou, M.F., Zhao, J.H., Zhang, K.J., Chen, W., 2008. Geochronology and geochemistry of the c. 80 Ma Rutog granitic pluton, northwestern Tibet: implications for the tectonic evolution of the Lhasa Terrane. Geol. Mag. 145, 845–857. https://doi.org/10.1017/s0016756808005025.
Zhu, D.C., Pan, G.T., Chung, S.L., Liao, Z.L., Wang, L.Q., Li, G.M., 2008. SHRIMP Zircon Age and Geochemical Constraints on the Origin of Lower Jurassic Volcanic Rocks from the Yeba Formation, Southern Gangdese, South Tibet. Int. Geol. Rev. 50, 442–471. https://doi.org/10.2747/0020-6814.50.5.442.
Zhu, D.C., Mo, X.X., Niu, Y.L., Zhao, Z.D., Wang, L.Q., Liu, Y.S., Wu, F.Y., 2009. Geochemical investigation of Early Cretaceous igneous rocks along an east–west traverse throughout the central Lhasa Terrane. Tibet. Chem. Geol. 268, 298–312. https://doi.org/10.1016/j.chemgeo.2009.09.008.
Zhu, D.C., Zhao, Z.D., Niu, Y.L., Mo, X.X., Chung, S.L., Hou, Z.Q., Wang, L.Q., Wu, F.Y., 2011. The Lhasa Terrane: Record of a microcontinent and its histories of drift and growth. Earth Planet. Sci. Lett. 301, 241–255. https://doi.org/10.1016/j.epsl.2010.11.005.
Zhu, D.C., Zhao, Z.D., Niu, Y.L., Dilek, Y., Hou, Z.Q., Mo, X.X., 2013. The origin and pre-Cenozoic evolution of the Tibetan Plateau. Gondwana Res. 23, 1429–1454. https://doi.org/10.1016/j.gr.2012.02.002.
Zhu, D.C., Wang, Q., Zhao, Z.D., Chung, S.L., Cawood, P.A., Niu, Y., Liu, S.A., Wu, F.Y., Mo, X.X., 2015. Magmatic record of India-Asia collision. Sci. Rep. 5, 14289. https://doi.org/10.1038/srep14289.
Zhu, D.C., Wang, Q., Cawood, P.A., Zhao, Z.D., Mo, X.X., 2017. Raising the Gangdese Mountains in southern Tibet. J. Geophys. Res. Solid Earth 122, 214–223. https://doi.org/10.1002/2016jb013508.
Zhu, D.C., Wang, Q., Chung, S.L., Cawood, P.A., Zhao, Z.D., 2019. Gangdese magmatism in southern Tibet and India-Asia convergence since 120 Ma. Geol. Soc. Spec. Publ. 483, 583–604. https://doi.org/10.1144/sp483.14.